

The copyright of this thesis vests in the author. No quotation from it or information derived from it is to be published without full acknowledgement of the source. The thesis is to be used for private study or non-commercial research purposes only.

Published by the University of Cape Town (UCT) in terms of the non-exclusive license granted to UCT by the author.

//

**GROWTH TEMPERATURE AND MICROSTRUCTURAL  
DIFFERENCES IN HYDROGENATED AMORPHOUS  
SILICON DEPOSITED ON GLASS SUBSTRATES**

Thesis submitted in partial fulfillment of the requirements for the degree of  
Master of Science in Physics

**Evariste Minani**

Department of Physics  
University of Cape Town

October 2002

## ABSTRACT

Hydrogenated amorphous silicon (a-Si:H) is an important thin film semiconductor with a wide variety of applications in microelectronics and optoelectronics. However, it is metastable and photodegrades after a moderate light illumination (Staebler- Wronski effect). The most stable material has been suggested to be at the edge of crystallinity with microcrystalline inclusions.

Using a combination of positron annihilation and X-ray diffraction techniques, the microstructure of hydrogenated amorphous silicon grown by hot wire chemical vapour deposition on glass substrates at different substrate temperatures ranging between 300 °C and 500 °C is examined. In previous studies the crystallisation was accompanied by a relaxation of defect structure with an increase in free volume at positron annihilation site. In this work, both techniques show a relaxation of the network with increasing growth temperature, leading to a higher degree of ordering, shorter bond lengths, and a reduction in the average size of defects in the material.

## ACKNOWLEDGEMENTS

I would like to express my sincere appreciation and gratitude to:

Prof. M. Härting and Prof. D.T Britton, my supervisors, for their continuous guidance and fruitful discussions throughout the proceeding of this work.

Dr. A. Hempel for her earlier assistance in the use of the positron LABS, Drs. M. Hempel and R.

Bucher and Mr.T.P. Ntsoane for their assistance during X-ray diffraction measurements

Charlotte, my wife; Ghislain and Joselyne, my kids, for being so much comprehensive

KIE for allowing me to continue my studies

# CONTENTS

<b>1-OVERVIEW OF KNOWLEDGE ON AMORPHOUS MATERIALS....</b>	<b>1</b>
1.1 Introduction.....	1
1.2-Structure and defects in amorphous material .....	1
1.2.1 Structure of amorphous solids.....	1
1.2.2 Defects in amorphous silicon .....	6
1.3 Properties of amorphous material.....	9
1.3.1 Electronic properties.....	9
1.3.2 Optical properties.....	16
1.4 Applications of amorphous material.....	18
1.4.1 Electronic applications.....	19
1.4.2 Optical applications .....	22
1.5 Conclusion.....	23
<b>2.INVESTIGATION TECHNIQUES.....</b>	<b>25</b>
2-1 Introduction.....	25
2-2 Diffraction techniques.....	25
2.2.1 Introduction.....	25
2.2.2 Derivation of the radial distribution density.....	27
2.3 Positron annihilation spectroscopy .....	31

2.3.1 Introduction .....	31
2.3.2 Fundamental of positron annihilation. ....	31
2.3.3 Momentum distribution techniques. ....	36
2.4 Conclusion.....	40
<b>3.EXPERIMENTAL TECHNIQUES.....</b>	<b>41</b>
3.1 Samples characteristics and growth conditions. ....	41
3.2 Positron beam at UCT. ....	43
3.3 X-ray phase analysis diffractometer at iThemba LABS .....	47
3.4 Measurements.....	49
3.5 Conclusion. ....	51
<b>4. RESULTS. ....</b>	<b>52</b>
4.1 X-ray diffraction results.....	52
4.2 Electron momentum spectroscopy.....	56
4.3 Conclusion.....	60
<b>5. DISCUSSIONS .....</b>	<b>61</b>
<b>6.GENERAL CONCLUSION.....</b>	<b>64</b>
<b>REFERENCES.....</b>	<b>66</b>
<b>APPENDIX.....</b>	<b>70</b>

## LIST OF FIGURES

- 1.1 Schematic illustration of the structural origin of certain features in the density function for an amorphous solid. (p.3)
- 1.2 Schematic illustration of the local structure in a-Si:H. (p.5)
- 1.3 Density of states in amorphous solid.  $E_v$  and  $E_c$  separate the localized and delocalised states in the conduction and valence bands. (p.12)
- 2.1 Scattering experiment (p.26)
- 2.2 The reduced radial distribution function of amorphous material. (p.30)
- 2.3 Scheme of different positron experiments. (p.36)
- 2.4 A Doppler broadened 511 keV peak measured for perfect silicon. The intervals used for defining the  $S$  and  $W$  parameters are indicated. (p.37)
- 2.5 The diagram of  $S$  vs  $W$  parameter for an amorphous silicon sample deposited on a silicon substrate. (p.39)
- 3.1 Different source/moderator configurations. (p.44)
- 3.2 Diagram of the positron beam at the University of Cape Town. (p.45)
- 3.3 X-ray phase analysis diffractometer. (p.47)
- 3.4 Schematic diagram of the experimental configuration for X-ray phase analysis measurements. (p.49)

- 4.1 X-ray diffraction pattern for a 2288 nm thick a-Si:H layer deposited on glass substrate at a substrate temperature of 400 °C. (p.52)
- 4.2 The radial distribution function for a-Si:H layers grown by HWCVD at different deposition temperatures ranging from 300 °C to 500 °C. (p.53)
- 4.3 Dependence of the nearest neighbour separation  $R$  on the deposition temperature for all a-Si:H layers grown by HWCVD at different glass substrate temperatures. (p.55)
- 4.4 Dependence of the bond angle on deposition temperatures for the a-Si:H layers deposited by HWCVD on glass substrate at different temperatures. (p.55)
- 4.5 Positron line shape parameter  $S$  measured as a function of the mean penetration depth for a 3367 nm a-Si:H layer deposited on glass substrate at 450 °C. (p.56)
- 4.6 Doppler broadening parameter  $W$  as a function of the mean depth penetration for a 3357 nm thick a-Si:H layer deposited by HWCVD on glass substrate at 450 °C. (p.57)
- 4.7 The  $S$ - $W$  map for the 3357 nm thick a-Si:H layer deposited by HWCVD on glass substrate at 450 °C. (p.58)
- 4.8 Dependence of the low momentum fraction  $S$  on growth temperature for different a-Si:H layers deposited by HWCVD on glass substrates. (p.59)
- 4.9 Dependence of the high momentum fraction  $W$  on growth temperature for different a-Si:H layers deposited by HWCVD on glass substrates. (p.60)
- 5.1 Correlation between low momentum fraction  $S$  and high momentum  $W$  for all a-Si:H layers deposited by HWCVD on glass substrate at different temperature between 300 °C -500 °C .(p.62)
- 5.2 Correlation between the nearest neighbour separation  $R$  and low momentum fraction  $S$  for all samples used in this study. (p.63)

## LIST OF TABLES

Table 3.1: The growth parameters and characteristics of the a-Si:H layers used in this study.

(p.42)

Table 4.1: Characterisation of the a-Si:H layers grown by HWCVD on glass substrate at different temperatures. (p.54)

University of Cape Town

# **CHAPTER 1**

## **OVERVIEW OF KNOWLEDGE ON AMORPHOUS MATERIAL**

### **1-1. Introduction**

Over the past thirty years, considerable efforts have been devoted to the understanding of the properties of amorphous materials. Amorphous silicon (a-Si) and hydrogenated amorphous silicon (a-Si:H) are particularly important due to their potential technical applications in microelectronics and opto-electronics such as solar cells, thin film transistors, optical sensors [1,2,3].

A detailed understanding of the physical and chemical properties of amorphous solid can be achieved only when the structural arrangement of atoms in such material is well known. Thus, the characterization of the structure of hydrogenated amorphous silicon will be the starting point to investigate such material.

In this chapter important results from previous studies on amorphous materials and particularly on hydrogenated amorphous silicon will be highlighted. Attention will be focused on the structure and defects in such materials, properties and applications will be also discussed.

### **1-2. Structure and defects in amorphous materials**

#### **1-2-1. Structure of amorphous material**

The atomic structure of amorphous materials, and especially hydrogenated amorphous silicon, has been investigated using diffraction techniques such X-ray [4], electron

[5] or neutron beams [6]. In contrast to the sharp diffraction patterns observed for crystalline material, amorphous materials yield diffuse diffraction patterns [1,3,7]. On one hand this is characteristic of the absence of a long-range order observed in crystalline solid, but on other hand this indicate that the structure of amorphous material is not random in the statistical sense and that a short range order holds on a certain scale.

The evidence of this is given by the radial distribution function (RDF), which is a correlation function between pairs of atoms obtained from the Fourier transform of the diffraction measurements. This function expresses the density of atoms or electron as a function of the radial distance  $r$  from any reference atom or electron in the crystal.

If it is assumed that the substance is composed of one kind of atoms, the radial distribution function is given by:

$$4\pi r^2 \rho(r) = 4\pi r^2 \rho_0 + \frac{2r}{\pi} \int k f(k) \sin kr dr \quad (1.1)$$

where  $\rho(r)$  is the density of atoms at a distance  $r$  from the reference atom,  $\rho_0$  the average density of atoms,  $k$  is the scattering vector

$$k = \frac{4\pi \sin \theta}{\lambda} \quad , \quad (1.2)$$

and  $f(k)$  the reduced scattering intensity

$$f(k) = \frac{I(k)}{Nf^2} - 1 \quad (1.3)$$

$N$  is the number of atoms,  $f$  the atomic scattering factor and  $I(k)$  the scattered intensity

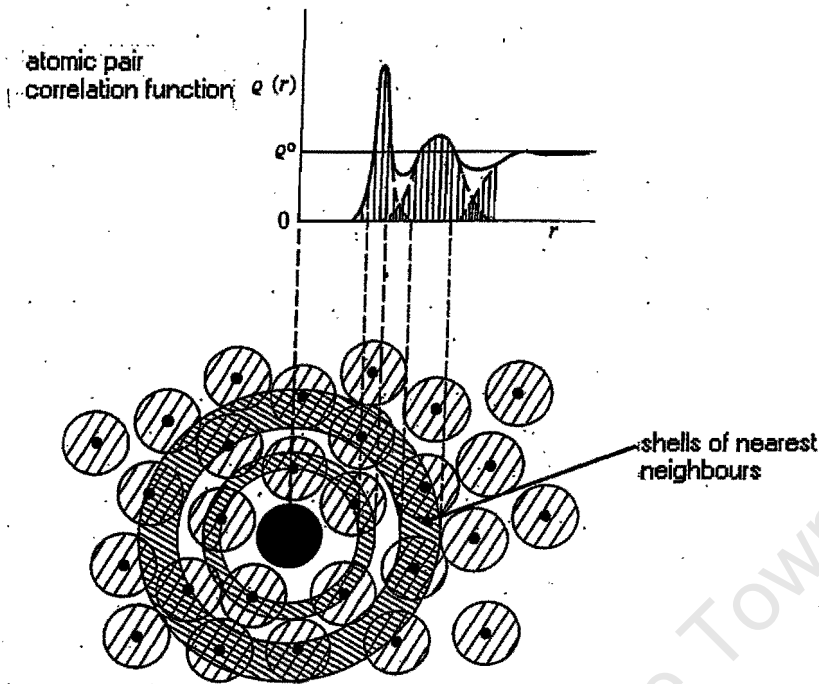


*Figure 1.1: Schematic illustration of the structural origin of certain features in the density function for an amorphous solid [3]*

The first peak in the radial distribution density is related to the interatomic distance, and the area under that peak with the coordination number. The second peak corresponds to correlation with the nearest neighbours and the area under this peak gives the number of second neighbours.

In the case of amorphous silicon [5], it has been shown that the first peak of the radial distribution function in amorphous silicon almost coincides with that of crystalline silicon even if a slight elongation (1%) can be detected. The area under the first peak was found to be the same for amorphous and crystalline silicon. The second peak, which gives the number of second neighbours, is broadened in the case of amorphous silicon and this is accounted for by the variation of the bond angle.

Thus, theoretically, the structure of hydrogenated amorphous silicon can be deduced from the structure of crystalline silicon (c-Si), which crystallises in the diamond structure. Atoms of silicon are linked by covalent bonds to four neighbours in a regular tetrahedron with only distortions in the bond angles and lengths [8]. The number of second nearest neighbours will be indeed twelve as it is in the case of c-Si.

Modelling the microscopic and the electronic structure of amorphous silicon and hydrogenated amorphous silicon, however, remained a considerable challenge in the field of computational physics. Those models of structure have been developed to fulfil the feature of the radial distribution function.

The first one to be considered was the microcrystalline model [8], which presents amorphous material as composed of microcrystallites. The expected density of dangling bonds in this model is greater than that observed.

The model proposed by Grigorovici [9], with a structural unit of dodecahedron, can account for RDF better than the microcrystalline model does, but there still remains discrepancies like the bond angle which is about  $108^\circ$ , a deviation from  $109^\circ 28'$  observed for tetrahedrally bonded materials.

The Continuous Random Network model (CRN) proposed by Polk [8] accounts for the RDF better than the previous models. In this model, dangling bonds are only created at the surface; the fluctuation of bond length and bond angle are within 1% and 10% respectively and finally the dihedral angles are chosen for distortion by bond angle and bond length to as small as possible.

Despite the effort done in this area to elucidate the real structure of amorphous solids there is no consensus about the exact structural model of amorphous material and the coexistence of both structures becomes more plausible.

Recent works on a-Si:H deposited by hot wire chemical vapour deposition using positron annihilation spectroscopy and X-ray diffraction techniques [10] have shown that the a-Si:H deposited on glass substrate at different substrate temperature forms a continuous random network and there was no evidence of microcrystalline phase.

So far we have discussed the structure of amorphous silicon as a perfect tetrahedrally bonded solid. In practice, however, the material only approximates this perfect amorphous structure with dangling bonds terminated by hydrogen and containing large open volume defects.

The local structure around hydrogen in a-Si:H has been investigated from steady state and pulsed neutron scattering measurements [3] and the two measurements have provided similar results. From the radial distribution function the distances of Si-Si, Si-H and H-H bonds have been calculated as shown in figure 1.2 [11] and a  $109.5^\circ$  tetrahedral angle was retained.

Data from infrared absorption measurements can provide information about the bonding modes of Si and H atoms [12] and the bonding scheme of hydrogen is likely to change with substrate temperature.

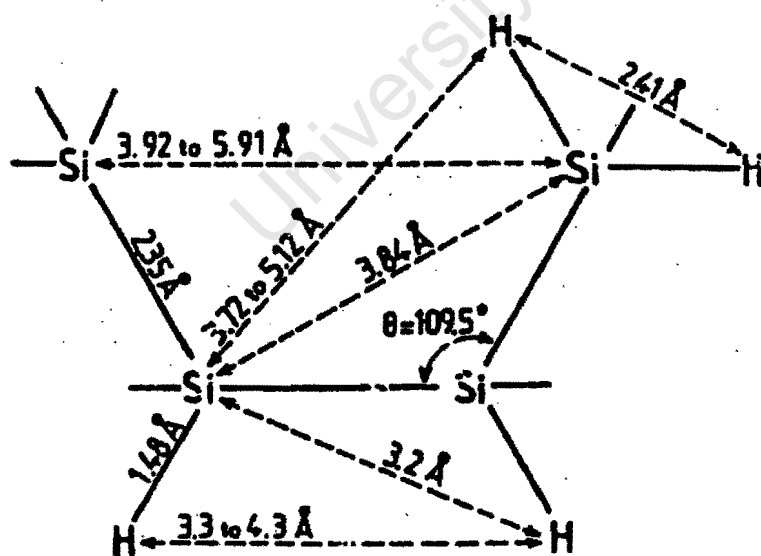


Figure 1.2: Schematic illustration of the local structure in a-Si:H [11]

## 1-2-2. Defects in amorphous materials

The actual samples on amorphous silicon have a structure deviating from the ideal continuous random network, namely, coordination of constituent atoms deviates from the normal coordination following the 8-N rule, where N designates the number of valence electrons. In the case of amorphous silicon, the normal coordination is fourfold, but there are present threefold coordinated silicon atoms. Such atoms are structural defects in amorphous semiconductors. Impurities or foreign atoms (e.g. hydrogen in a-Si:H ) give rise to additional disorder in the amorphous network

Different experimental methods have been used to obtain information about structural defects. Among them electron spin resonance (ESR) [13] provides with information about the nature of defect while the energy position of defect levels in the band gap region is estimated from spectroscopic means. Optical spectroscopy such as photo-induced absorption [14] and photo-thermal deflection spectroscopy [15] measure optical transition energy, namely, the depths of defect level are optically estimated.

### a- Coordination defects

Under-coordination defects in covalently bonded material are basically dangling bonds. They are typical examples for defects in tetrahedrally-bonded amorphous semiconductors such as a-Si:H. Dangling bonds in these materials have been extensively investigated using various kind of measurements and were found to be consistent with structural defects whose charge state can be neutral, positive or negative [16]. The density of dangling bonds in a-Si:H can be varied depending on the substrate temperature, the hydrogen content and other preparation conditions.

The presence of hydrogen related dangling bonds, *i.e.*, a dangling bond having hydrogen at nearby site has been suggested from electron-nuclear double resonance (ENDOR) measurements in a-Si:H [17]. The position of the energy level of dangling bonds in a-Si:H has been estimated by various kinds of measurements. The neutral dangling bond level is located almost in the mid gap [16], but there still controversy on its exact position in the band gap. The measured depth level of the negatively charged dangling bond is divided into two intervals: 0.5 - 0.6 eV and 0.8 - 0.9 eV [18] and these values depend on hydrogen content of the sample.

Prolonged illumination creates dangling bonds and in a-Si:H it can only involve the breaking of Si-H or Si-Si. The breaking of weak Si-Si bonds by prolonged illumination seems to be the major mechanism for the light induced defect creation in a-Si:H as the energy required to break the Si-H bond of about 3.5 eV can only be achieved when the undoped a-Si:H is bombarded with energetic particles or when the material is annealed at temperature above 400 °C. The bond breaking is triggered by nonradiative recombination of electrons with holes trapped at such weak Si-Si bond [19]. But there is also a model in which the threefold-coordination silicon centres with negative correlation energy may capture an electron or a hole to form a neutral dangling bond under optical excitation [2].

Over-coordinated defects are less common and may arise when an additional covalent bond is formed between a normally coordinated atom and another. This type of defects in a-Si:H has been proposed, as the hydrogen interacting interstitially with weak Si-Si bonds [20]

## **b- Atomic vacancies**

These are another form of defects in hydrogenated amorphous silicon semiconductors. They are responsible for many of the electrical and optical properties of such material. Vacancies can be thermally generated but are also created by irradiations damage processes such as displacement damage processes when an incident particle of radiation ( $\gamma$  ray photons or neutrons) with sufficient energy displace an atom of silicon by breaking bonds or electronic rearrangement when a radiation causes an electronic excitation [3]. In this case electrons or holes resulting from this excitation can either be trapped at a pre-existing defects or can cause bonds to break thereby creating neutral dangling bonds. Atomic vacancies may occur either singly as monovacancies or as clusters, divacancies. They are, after the single dangling bonds defects, the most simple form of structural defects likely to be found in a-Si:H.

## **c- Density defects**

This is another form of defect, which can be found in amorphous semiconductors. These defects range from voids, which may be regarded as an aggregate of a non fixed number of vacancies, to fluctuation in density (or free volume) which may be regarded as vacancies which have become distributed throughout the material and which therefore cannot be regarded any more as a well-defined point defects.

The presence of such defects influences to a great extent the physical properties of the material because of the dangling bonds that are expected at the void surface, and although annealing the samples to elevated temperatures does reduce the voids concentration to a certain extent, they cannot be removed entirely before the crystallization temperature is reached [1].

The annealing behaviour of defects structure in hydrogenated amorphous silicon produced by hot wire chemical vapour deposition has been studied by pulsed and conventional positron beam techniques combined with X-ray diffraction. An annealing stage, below the growth temperature, was found to lead to an increase in open volume and this was related to a redistribution of hydrogen in the sample and its escape from it [10]

The importance of defects in amorphous material lies in the fact that many properties of amorphous material can be defect controlled. In many case the behaviour resulting from the presence of defects can completely dominate that due to the intrinsic material.

## **1.3 Properties of amorphous material**

### **1-3-1 Electronic properties**

The structure of hydrogenated amorphous silicon is characterized as irregular arrangement of atoms in contrast with the crystalline silicon whose structure has a periodic array of atoms. Although the long-range order is broken the short range order is retained and this feature is reflected in their electronic properties

#### **a- Electronic density of states**

The chemical bond theory provides with a simple physical understanding of the electronic structure of crystalline semiconductors as the valence band is thought to be solely constructed from the bonding orbitals while conduction band is obtained from anti-bonding

orbitals. In that case electron states are defined by a Bloch waves extending throughout the crystal [1]

$$\Psi(k, r) = u(k, r) \exp(ikr) \quad (1.4)$$

where the function  $u(k, r)$  has the periodicity of the crystal lattice in which a lattice translation vector  $R$  connect lattice points.

$$u(k, r + R) = u(k, r), \quad (1.5)$$

this function modulates the exponential term representing the plane wave.

The allowed wave vectors are related to the symmetry of the crystal lattice and a reciprocal lattice (or  $k$ -space) can be established. The allowed energies of electrons are thus represented by the means of band structure in  $k$ -space

The absence of periodicity in amorphous solids does not allow the electron states to be represented by a band structure in the form of

$$E(k) = \frac{\hbar^2 k^2}{2m} \quad (1.6)$$

But evidence of the band structures in a perfect amorphous solid was given by Weaire and Thorpe [21], considering that the short-range order holds in such materials and that this, mainly, determines the electronic density of states. The gap in the density of states was also proved. Actual profiles for the valence and the conduction bands can be obtained from X-ray photoemission spectroscopy and X-ray inverse photoemission, respectively.

The presence of disorder in amorphous material affects these band structures. The fluctuation in the bond length, bond angle and dihedral angle inherent to the continuous random network in amorphous solid was found to give rise to the shift of the band edge. The tail states arising from such fluctuations were found to have a localized character [22]. If an electron in

amorphous material is considered as subjected to the potential fluctuation associated with disorder the critical condition for localization – delocalization is that the potential fluctuation is comparable with the bandwidth  $B$  of the Bloch state without the potential fluctuation.

$$B = 2zI \quad (1.7)$$

where  $I$  is the transfer integral and "  $z$  " the coordination number.

The separation between these states can be physically understood in the way that the energy level is distributed by the potential fluctuation. Thus, the energy level at the band tail region is low compared to the central region of the band. This means that the states of the same energy in the band tail region are well separated in the lattice, so that the tunnelling probability between these sites becomes small. Thus the state becomes localized. The boundary between localized and delocalised states is called mobility edge, and the wave function of the extended state changes when its energy crosses the mobility edge.

Time of flight (TOF) measurements [23] estimated the width of the conduction band tail to be 25 meV for standard a-Si:H samples and photoemission yield measurements [24] estimated the valence band tail width to 51 meV while Urbach tail measurements yield a valence band tail of 48 meV from the same sample [25]. This is reasonable as the wave function of the conduction band tail is more extended than that of the valence band tail so that the former wave function is not so much affected by spatial fluctuations of bonds lengths, bond angles dihedral angles etc. compare to the latter wave function.

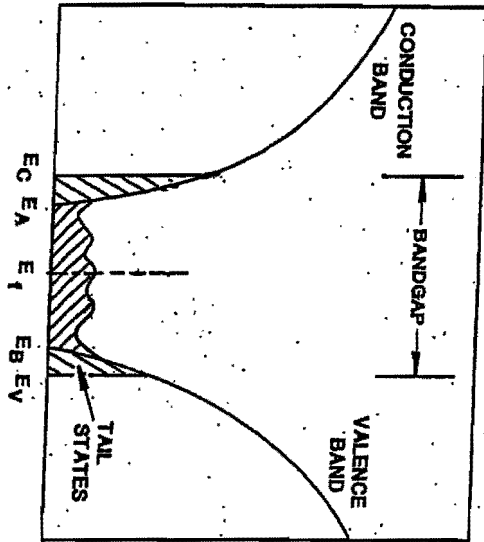


Figure 1.3: Density of states in amorphous solid.  $E_v$  and  $E_c$  separate the localized and delocalised states in the conduction and valence bands [1].

The density of localized states within the mobility gap was found to be low for a-Si:H and was critically controlled by the deposition temperature of the substrate [1]. This low density of localized states enables them to be doped either n or p-type and consequently to increase their conductivity.

## b- Electrical transport

The density of localized states inherent to defect in amorphous systems leads to different electrical transport processes.

### **b-1-Conductivity in extended states**

The conductivity in extended state occurs via carriers excited beyond the mobility edge into states at or above  $E_c$  (below  $E_v$ ). The conductivity for n-type conduction in that region can be expressed by [1]

$$\sigma = \sigma_{\min} \exp\left(-\frac{E}{k_b T}\right) \quad (1.8)$$

where  $\sigma_{\min}$  is the minimum metallic conductivity which is the smallest non-zero value of the conductivity at  $T = 0$  and  $E$  is the activation energy

### **b-2 -Conductivity in the tail**

The tail states generated by disorder, lie in the energy ranges  $E_a < E < E_c$  and  $E_v < E < E_b$ , for the conduction and the valence bands respectively. The conductivity at an arbitrary energy for n-type conduction is given by [1]

$$\sigma = e\mu g(E_x) k_b T \exp\left(-\frac{E_x - E_f + W}{k_b T}\right) \quad (1.9)$$

where  $\mu$  is the hopping mobility estimated from the diffusion coefficient,  $W$  the energy difference between the states,  $E_f$  the Fermi level and  $g(E_x)$  is the density of states.

### **b-3 - Hopping conductivity**

Hopping conduction means the transport of localized electrons, which hop from site to site with the assistance of phonons.

In p-type semiconductors, there are few donors and in n-type semiconductors, there are few acceptors, so that some acceptors or some donors are ionised. At the same time ionised

acceptors or donors are created with the same numbers as ionised donors or ionised acceptors. By such ionised impurities, the energy levels for donors in n-type semiconductors is affected by potential fluctuations and electrons hop between these fluctuating levels by emitting or absorbing phonons. The temperature dependence of the hopping conductivity,  $\sigma_h$ , due to nearest neighbour hopping is given by [2]

$$\sigma_h = \sigma_{ho} \exp\left(-\frac{\epsilon_3}{k_b T}\right) \quad (1.20)$$

where the pre-exponential factor  $\sigma_{ho}$  is closed to the minimum metallic conductivity and  $\epsilon_3$  is the activation energy which almost corresponds to the magnitude of potential fluctuation of the donor's levels for hopping electrons.

In amorphous semiconductors, hopping conduction occurs through unoccupied localized levels near the Fermi level. The existence of this type of conductivity was first pointed out by Mott [1] and is called variable range hopping. It can be understood if we consider the localized levels as distributed quasi-continuously.

For two sites between which the transfer integral is small, but whose energy difference  $W$  is small, the hopping probability increases with a factor of  $\exp\left(-\frac{W}{k_b T}\right)$ . Thus, electrons hop to the most probable sites.

In real materials, which may contain a high concentration of defects, and consequently have a high density of states in the gap, electron transport can take place via such defect states and the magnitude of defect conductivity may greatly exceed that due to the conventional band conduction.

A light induced effect on dark conductivity in which the dark conductivity decreases by four orders of magnitude has been observed by Staebler and Wronski [26] in a-Si:H. Such a

change is due to the shift of the Fermi level toward the valence band edge associated to the change in the density of states resulting from the creation of defects, consisting of dangling bonds which act as recombination centres, by prolonged illumination.

## 1-3-2 Optical properties

### a- optical absorption

The optical properties of a material are defined by the spectral dependence of its complex index of refraction,  $\varepsilon_r = \chi(E) + i\delta(E)$  where  $\chi$  is the refractive index and  $\delta$  is the absorption index [1]. The spectral region of major interest in semiconductors is in the vicinity of the absorption edge since it can provide information on the optical gap. In the case of hydrogenated amorphous silicon when the density of state is assumed to be parabolic, the optical gap  $E_{og}$  can be deduced from the expression below [2]

$$(\alpha\hbar\omega)^{\frac{1}{2}} = B^{\frac{1}{2}}(\hbar\omega - E_{og}) \quad (1.21)$$

where  $\alpha$  is the absorption coefficient  $\hbar\omega$  is the photon energy and  $B$  is a factor independent of  $\omega$  [1],

$$B = \frac{4\pi\sigma_{min}}{ncE} \quad (1.22)$$

where  $\sigma_{min}$  is the minimum metallic conductivity,  $c$  is the velocity of the light and  $E$  is the extent of band tailing.

Using these equations for a-Si:H the optical band gap was found to be in the range 1.7-1.8 eV and this result was found to be consistent with the theoretical predictions [27]. The change of the

exponential slope in the tail absorption due to prolonged illumination has been observed and has been attributed to an increase in the disorder of the amorphous network [28].

## **b. Photoluminescence**

Photoluminescence is a useful experimental means for investigating the nature of gap state and recombination processes in amorphous semiconductors.

In a-Si:H a band to band photoluminescence could occur. Electron-holes pairs created optically by photons having energy comparable to the band gap would also recombine radiatively directly emitting a photon of energy also comparable to the band gap [3]. Often, however, photoluminescence spectra are observed at energy considerably lower than the energy of the exciting photons, and electrons in the gap are often involved. These states are the band-tail states associated with structural defects, mainly dangling bonds. One possible mechanism for radiative recombination which gives rise to photons emitted at a significantly lower energy than those of exciting radiation are that an electron excited from the valence band into the conduction band will recombine with defects states deep in the gap, or the excited electron may thermalize down in the energy through deep lying localized tail states until recombination occurs with a hole trapped at a comparable deep valence band tail states [3].

The change in photoluminescence has been observed after a prolonged illumination and seems to be enhanced at low temperature illumination compared to illumination at room temperature [29].

## **c-Photoconductivity**

We are concerned with the photoconductivity based on currents flowing along external circuit through two ohmic contacts by photocarriers created under optical excitations.

In the presence of photoexcitation the conductivity  $\sigma_{ph}$  is expressed by [1]

$$\sigma_{ph} = e(\mu_n n + \mu_p p) - e(\mu_n n_o + \mu_p p_o) \quad (1.23)$$

where  $n$  and  $p$  are the electron and holes carriers concentrations under optical excitation respectively.

$\mu_n$  and  $\mu_p$  the conductivity mobilities of electrons and holes, and  $n_o$  and  $p_o$  the thermal equilibrium concentration in the dark.

In order to study the characteristic of semiconductors material it is convenient to express the number of free carriers

$$n = G\tau_n \text{ or } p = G\tau_p \quad (1.24)$$

where  $\tau_n$  or  $\tau_p$  is the lifetime of free carriers (electron or holes ) and  $G$  the volume generation rate of photocarriers.

When a film of thickness  $D$  is used and multiple reflection of absorbed light is negligible,  $G$  is given by [2]

$$G = N_o \eta (1 - R) \{1 - \exp(-\alpha D)\} \quad (1.25)$$

where  $N_o$ ,  $R$ ,  $\eta$  and  $\alpha$  are the number of incident photons per unit area, reflectivity, quantum efficiency and absorption coefficient.

The photocurrent is defined as the difference between the total current under optical excitation and the current in the dark when one type of photo-carriers are concerned.

$$I_p = e\mu E \Delta n \quad (1.26)$$

where  $\mu$ ,  $E$ ,  $\Delta n$  denote respectively free electron mobility, electric field and an excess-carriers density. Under steady-state excitation

$$\Delta n = G\tau \quad (1.27)$$

By measuring the amplitude and the phase shift of modulated photocurrents, one can evaluate the energy distribution of gap states and also elucidate the recombination and trapping processes involved in photoconduction [30].

A decrease in the photoconductivity due to the Staebler-Wronski effect has been observed and was related to the change in dangling bonds defects.

## **1-4 Applications of amorphous materials**

Silicate glasses were the only type of amorphous materials commonly used; the relatively recent discovery that very many other types of material can be produced in amorphous form, either as bulk glasses or as thin films, has led to a very rapid expansion in the use of such material in electronics, magnetic, and optical applications.

Amorphous semiconductors have many advantages over their crystalline counterparts where applications are concerned:

The low density of localized states in the mid gap allow them to be doped either n or p-type and this leads to an increase in conductivity.

The high photoconductivity, the ability to alloy with C or Ge to tune the band gap, a direct band gap and the ability to be deposited at over large areas afford them many applications in microelectronics and opto-electronics. In this part some of the more important technological applications of hydrogenated amorphous silicon are surveyed.

## 1-4-1 Electronic applications

### a. Solar cell

A direct conversion of sunlight to electrical power is one of the most technologically developed and potentially the most important application of hydrogenated amorphous silicon. It is attractive from the energy point of view as it represents a potentially inexhaustible source of energy.

The ideal energy conversion efficiency  $\eta$  of the solar cell is defined by [1]

$$\eta = \frac{j_{sc} V_{oc} ff}{P_{in}} \quad (1.28)$$

where  $j_{sc}$  is the short circuit current density,  $V_{oc}$  the open circuit voltage,  $P_{in}$  the incident power and  $ff$  is the fill factor.

$V_{oc}$  is generally limited by the direct band-to-band recombination of photo-generated carriers. However a non-uniform density of states within the mobility gap, inherent to amorphous material, leads to recombination via these defects states and provide an upper limit to  $V_{oc}$ .

The fill factor is given by [1]

$$ff = \frac{I_m V_m}{j_{sc} V_{oc}} \quad (1.29)$$

where  $(I_m, V_m)$  is the maximum power point on the solar cell current- voltage characteristics.

The conversion efficiency of a practical solar cell is limited by the intrinsic or extrinsic losses due to the inability of a cell with a band gap  $E_{og}$  to properly match the broad solar spectrum or an incomplete extraction of photo-generated carriers and non-radiative recombination of carriers.

As Henry [31] showed, the theoretical maximum efficiency of an ideal photovoltaic cell reaches 31% for a semi-conducting material with a band gap of 1.35 eV, although material with gaps in the range 1-2 eV are predicted to have ideal photovoltaic efficiencies higher than 25 %. These calculations are based on AM1.5 illumination conditions.

The solar illumination intensity,  $P_{in}$ , is  $100 \text{ mWcm}^{-2}$  at sea level on a clear sunny day with the sun at the zenith, and is termed AM1[1]. The AM1 spectrum peaks at a wavelength of  $0.5 \mu\text{m}$ , which matches the absorption edge of a-Si:H better than that of crystalline silicon: since the edge of c-Si, due to indirect optical transitions, lies considerably below that of a-Si:H. This means that a film of a-Si:H only a few micrometers thick will absorb most of the useful sunlight, whereas a thickness of several hundred micrometers of c-Si is required to do the same.

Although AM1 photovoltaic efficiencies of c-Si solar cell of 24% [32] have been achieved, *i.e* approaching the ideal limit, this material is not suitable for large-scale applications even if crystalline cells of about 15% efficiency represent about 90% of world PV sales [33]. a-Si:H films, can readily be deposited onto large area substrates, and can even be deposited onto a continuous flexible substrate. Thus, although the photovoltaic efficiency of a-Si:H ( $\leq 10\%$ ) is considerably lower than that of its crystalline counterparts, this deficiency is ameliorated to a considerable extent by the fact that large area films of a-Si:H can be produced relatively cheaply.

In addition to the intrinsic loss experienced even by an ideal cell as a result of mismatch between the optical absorption characteristic of the semiconductor and the solar spectrum, actual solar cells suffer a number of additional loss processes such as reflection losses, incomplete

extraction or non-radiative recombination of photo-generated electrons and holes, and series resistance effects. This limits the maximum efficiency of a simple a-Si:H solar cell to about 10%, unless more complicated geometries ( tandem cell ) are used. [3]

A degradation of the performance of solar cells due to the light induced defects (Stabler-Wronski effect) discussed earlier is a limiting factor for the use of solar cells.

### **b-Electrophotographic application**

Hydrogenated amorphous silicon has another application in the field of electrophotography or xerography in document copying machines [3]. The material which was firstly used in that context was a-Se in thin film form and recently a-Si:H films have been utilized instead [34] as the photo-receptor.

Certain conditions must be met for a material to be a suitable photoreceptor. It must be able to be produced in defect-free large areas, and the material must be mechanically robust and chemically inert, in order to withstand, both abrasion and chemical degradation in the presence of intense light and electrical field respectively.

As far as electrical properties are concerned the material must be highly resistive ( $\rho \geq 10^{12} \Omega.cm$ ) in order that the surface potential does not decrease appreciably before or after light exposure.

The direct current resistivity of hydrogenated amorphous silicon is insufficient and a passivation layer is needed on the top surface of a-Si:H photoreceptor to immobilize the charge injected into it from the photoconducting a-Si:H layer below. This disadvantage is outweighed by the advantage it has over previous a-Se photoreceptor, namely in having extremely high surface hardness, non-toxicity and high optical sensitivity and a low price as well.

### **c- Thin film transistors**

The material requirement of the semiconductors in thin film transistors (TFT) are that the resistance of the TFT in the on state should be small enough for the capacitor formed by the liquid-crystal pixels element to be charged adequately. Moreover the resistance in the off state should be sufficiently high to keep the stored charge. Hydrogenated amorphous silicon fulfils these requirements. However, even if its dark conductivity is low enough to preclude charge-leakage effects, the material has such a high photoconductivity that the TFT element needs to be masked from any illumination [3]. The low carrier mobility of hydrogenated amorphous silicon limits the dynamic performance of TFTs unless very small channels widths are used.

## **1-4-2 Optical applications**

### **Light emitting diodes**

The light emitting diodes is one of the recent works on active optical device utilizing hydrogenated amorphous silicon. As mentioned above, the low density of localizes state in a-Si:H enable them to be doped n- or p-type and so, in principle, diodes based on this material could be made to exhibit electro-luminescence resulting from radiative recombination of electrically injected carriers.

Except for these important applications for a-Si:H discussed above there are many other small applications whenever human-scale application of a semiconductors is needed. We can mention photovoltaic cell for calculators, watches, batteries chargers, photo conductor for colour sensors or light sensors, anti-reflecting/ antistatic layer for televisions etc.

## I-5 Conclusion

In this chapter, we have presented a survey of important results from studies conducted on amorphous material in general and particularly on hydrogenated amorphous silicon.

The structure of a-Si:H deposited by hot wire chemical vapour deposition was found to consist of a continuous random network. Atoms of silicon are linked covalently to four nearest neighbours in regular tetrahedron with small distortion in the bond length and bond angle.

Structural defects consisting of dangling bond defects, atomic vacancies in the form of monovacancy or divacancy are likely to be found in a-Si:H. These defects, responsible for many of the electrical and optical properties of that material, were related to the deposition conditions such as the temperature of the substrate or hydrogen content of the sample.

Important properties, in connection with the applications of a-Si:H have been mentioned.

The low density of localized states allow them to be doped either n- or p-type, the high photoconductivity and a direct band gap are useful properties where applications are concerned.

The ability to be produced in homogeneous large area makes them a good choice in solar cell, thin film transistors, electrophotography, and light emitting diodes industries.

The photodegradation due to a prolonged illumination, known as the Staebler-Wronski effect, affects a-Si:H by increasing the number of dangling bonds in such material. This effect has become the biggest handicap for the widespread use of that material in solar cells. A stable material has been suggested to be at the edge of crystallinity with microcrystalline phase inclusions [35,36].

The aim of this work is to relate the initial defect configuration to the degree of order in the structure of a-Si:H samples deposited by HWCVD on glass substrate at different temperatures under otherwise identical conditions.

This thesis is organized as follows: after this overview of knowledge on amorphous material, the second chapter discuss the techniques used to investigate the formation of the microcrystalline phases and structural defects in amorphous solids and the third chapter is focussed on how these techniques were exploited and on how our measurements were conducted at UCT, for positron annihilation spectroscopy, and iThemba LABS for X-ray diffraction measurements. The fourth chapter presents the experimental results from different measurements and the fifth chapter gives a detailed interpretation of these results in relation to the theoretical prediction of defects structure and microcrystalline phases in a-Si:H. A general conclusion summarizes the important results and suggestions on how further work on the material may be oriented.

# **CHAPTER 2**

## **INVESTIGATION TECHNIQUES**

### **2-1 introduction**

The preceding chapter was dedicated to the understanding of the structure and defects in amorphous material. Important properties related to different applications of that material were also summarized.

Different techniques have been used to investigate the structure and defects in amorphous material [1,2], but only a few characterisation techniques are sensitive enough on an atomic scale. Among them, X-ray diffraction techniques [4] and positron annihilation spectroscopy [37] have proved to be very useful on that scale. Both techniques allow non-destructive measurements and high sensitivity range. In this second chapter, the theoretical basis behind these experimental techniques will be discussed for a better understanding of the experimental results.

### **2-2 Diffraction techniques**

#### **2-2-1 introduction**

X-rays are transverse electromagnetic waves. The diffraction of X-rays by matter results from a scattering process, in which X-rays are scattered by the electrons of atoms, and the interference between the scattered waves. The diffracted beam is observed only when certain geometrical conditions are satisfied, which may be expressed by the Bragg law for crystalline material.

$$2d_{hkl} \sin \theta = n\lambda \quad (2.1)$$

where  $d_{hkl}$  is the spacing of the lattice,  $2\theta$  the scattering angle,  $n$  an integer and  $\lambda$  the wavelength of the radiation.

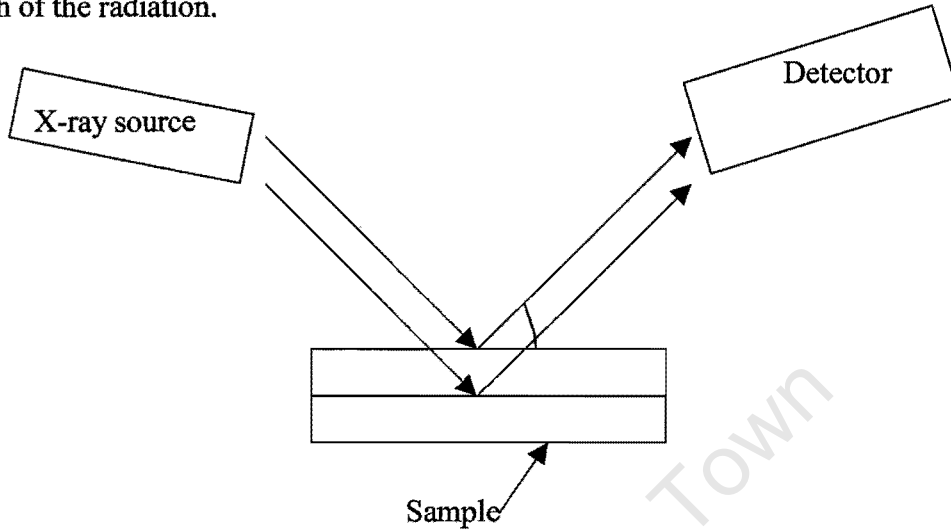


*Figure 2. 1: Scattering experiment*

In the case of crystalline solids, the resulting diffraction patterns comprising both the position and intensities of the diffraction effects are used for the identification of the substance and the determination of its complete structure [38]. Analysis of these positions and intensities leads immediately to the knowledge of the position of the individual atoms in the cell, and also the size, the shape, and the orientation of unit cell.

In the previous chapter it was mentioned that in contrast to the sharp diffraction patterns associated with the long range order in crystalline materials, only one or more broad diffuse haloes are generated by amorphous solids. This was understood as the interference between waves scattered by individual electrons or atoms not being fully constructive or destructive due to the lack of any overall structural regularity in such materials. This has a direct consequence

that the available intensity information may be used for the determination of the magnitude of the interatomic vectors but not their directions.

The results from the X-ray diffraction experiments on amorphous solids can be represented using a radial distribution function, which was found to be a very useful representation of the topology of an amorphous network [39]. This section presents a theoretical derivation of the radial distribution function and the accuracy of the information carried out from that function is also discussed.

### 2-2-2 The derivation of the radial distribution density

The basis for radial distribution analysis is the Debye equation [40], which expresses the intensity, as a function of the scattering vector  $k (= \frac{4\pi \sin \theta}{\lambda})$ , scattered by non-crystalline arrays of atoms at the angle  $\theta$ ,

$$I(k) = \sum_n \sum_m f_m f_n \frac{\sin kr_{mn}}{kr_{mn}} \quad (2.2)$$

wherein  $f_{m,n}$  are the respective atomic scattering factors of the  $m$ th and  $n$ th atoms, and  $r_{mn}$  is the magnitude of the vectors separating two atoms. The double summation is taken over all pairs of atoms in the ensemble. In this equation it is assumed that the material is isotropic so that the vector  $r_{mn}$  may adopt all orientations with equal probability and that is true for amorphous materials.

If it is assumed that the material is monoatomic with the density function  $\rho$ , a new expression for the intensity scattered by such arrays of  $N$  atoms is [7],

$$I(k) = Nf^2 \left( 1 + \int_0^\infty 4\pi r^2 \rho(r) \frac{\sin kr}{kr} dr \right) \quad (2.3)$$

where  $4\pi r^2 \rho(r)$  is called radial distribution function. In equation (2.3), the distribution of atoms about any reference atoms is regarded as continuous function and the summation has been replaced by an integral.

Let us introduce  $\rho_0$  the macroscopic density. In the case of amorphous materials, the quantity  $(\rho(r) - \rho_0)$  will tend to zero for distances greater than a few primary atomic separations, and this consideration transforms the previous equation into:

$$I(k) = Nf^2 \left( 1 + \int_0^{\infty} 4\pi r^2 [\rho(r) - \rho_0] \frac{\sin kr}{kr} dr \right) \quad (2.4)$$

where the infinite upper limit is justified since the size of the sample in such experiments is much greater than atomic dimensions.

Finally, the introduction of the reduced scattering intensity  $f(k)$  and the reduced radial distribution function  $G(r)$  defined as follows:

$$f(k) = k \left( \frac{I}{Nf^2} - 1 \right) \quad (2.5)$$

and

$$G(r) = 4\pi r [\rho(r) - \rho_0] \quad (2.6)$$

into equation (2.4) yields the following expression:

$$f(k) = \int_0^{\infty} G(r) \sin kr dr \quad (2.7)$$

The importance of this equation is that the quantity  $f(k)$  is directly obtainable from experiment while the function  $G(r)$  describes the real space structure of the amorphous solid.

The Fourier transform of that equation leads to the expression below

$$G(r) = \frac{2}{\pi} \int_0^{\infty} f(k) \sin kr dr \quad (2.8)$$

Since the range of values of  $k$  accessible to experiments is strictly limited, errors may occur in the conversion of reciprocal space data to the real space correlation function via Fourier transforms. In the case of  $\text{CuK}\alpha$  radiation, used in our experiments ( $\lambda=1.54 \text{ \AA}$ ), the maximum value of  $k$ ,  $k_{max} = 8.2 \text{ \AA}^{-1}$  when a perfect transformation between reciprocal space and real space required an infinite range of  $k$  values according to the equation (2.8). This has a direct consequence of introducing what are called termination errors as  $f(k)$  is seems to be multiplied by a modification function  $M(k)$  which is equal to 1 for  $k < k_{max}$  and 0 for  $k > k_{max}$ .

$$G'(r) = \frac{2}{\pi} \int_0^{k_{max}} f(k) \sin kr dr = \frac{2}{\pi} \int_0^{\infty} f(k) M(k) \sin kr dr \quad (2.9)$$

The effect of this is the loss in resolution since small wavelengths in real space are lost.

The radial distribution function for amorphous materials exhibits an oscillatory behaviour [3] with the peak in the probability function representing the average interatomic separation. The position of the first peak gives a value of the average nearest neighbour bond length  $r_1$  and similarly the position of the second peak gives the next nearest neighbour distance  $r_2$ . The bond angle  $\theta$  can be deduced from these distances as expressed below

$$\theta = 2 \sin^{-1} \left( \frac{r_2}{2r_1} \right) \quad (2.10)$$

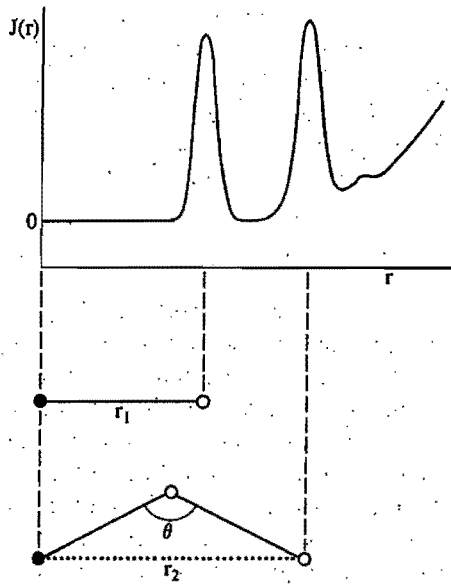


Figure 2.2 the reduced radial distribution function of amorphous material [3].

The importance of the radial distribution analysis lies in the fact that samples prepared in almost the same conditions, and consequently yielding similar diffuse haloes, may show differences in the radial distribution function and thus small structure details can be identified. However, it is a one-dimensional representation of three-dimensional structure and can therefore carry a limited amount of structural information even if isotropy and homogeneity are assumed in an amorphous sample of high quality.

## **2-3 Positron annihilation spectroscopy**

### **2-3-1 Introduction**

The early experiments with positrons were dedicated to the study of the electronic structure in metals and alloys. It is only at the end of 1960s that the annihilation parameters were found to be sensitive to the lattices imperfections and since the investigation of defects has become the dominant issue of positron annihilation spectroscopy [41].

The detection of defects by positron annihilation spectroscopy is based on their ability to capture positrons. The trapping of positron in defects is based on the formation of an attractive potential at open volume defects, such as vacancies, dislocations *etc* due to the lack of a repulsive positively charged ion core in such defects.

In this section the fundamentals of positron annihilation spectroscopy will be presented and the principle of different positron techniques will be summarized. Attention will be focussed on the Doppler broadening technique used in our experiments.

### **2-3-2. Fundamentals of positron annihilation**

#### **2-3-2-1 The positron**

The positron is the antiparticle of the electron. It has the same characteristics but the opposite charge and magnetic moment. It is stable in a vacuum with a lifetime  $\tau \geq 2 \times 10^{21}$  years [39], but interacts with electrons in matter and annihilates rapidly converting the total energy in radiant gamma rays. In this case the positron lifetime is only of few hundred pico-seconds [42]

Mainly positrons are emitted from the  $\beta^+$  decay of radioactive isotope like  $^{22}\text{Na}$ ,  $^{64}\text{Cu}$ ,  $^{19}\text{Ne}$ , and  $^{58}\text{Co}$  but positrons can also arise from the inverse of annihilation process. In that case, an energetic gamma ray passing near a heavy nucleus, that serves as catalyst, simply disappears, converting its radiant energy into the creation of an electron and a positron in a pair production process.

The choice of the source of positron is governed by the nature of the experiment to be made, its efficiency, the half-life and the facility to be handled. The most used is the  $^{22}\text{Na}$  isotope as it provides a good compromise between cost and half-life of 2.6 years [42]

### 2-3-2-2 Implantation, trapping and annihilation of positron

Once positrons have reached the surface of the sample they may be scattered back or may penetrate the sample. The backscattered positrons annihilate outside the sample leading to the distortion of the spectra. Special care must be taken in slow positron beam experiments to avoid the recording of such annihilation events.

Positrons which are not backscattered at high energy in the vacuum rapidly lose the high kinetic energy by undergoing inelastic collisions and diffuse through the sample until annihilation with electrons in the sample.

#### a-Implantation profile

The implantation profile  $P(z, E)$  of a monoenergetic positrons having energy  $E$  is given by the Makhovian profile [41]

$$P(z, E) = \frac{mz^{m-1}}{z_0^m} \exp\left(-\left[\frac{z}{z_0}\right]^m\right) \quad (2.11)$$

where

$$z_0 = \frac{\bar{z}}{\Gamma(1 + \frac{1}{m})}, \quad (2.12)$$

and the mean penetration depth is a function of incident positron energy  $E$

$$\bar{z} = A \frac{E^n}{\rho}. \quad (2.13)$$

$m$ ,  $n$  and  $A$  are empirical shape parameters,  $\rho$  the target mass density and  $\Gamma$  the gamma function.

The widely used values are  $A=4.0 \mu\text{gcm}^{-2}\text{keV}^n$ ,  $m = 2$  and  $n = 1.6$  [43]

The implantation profile of positrons reflects the depth of defects inside the sample. The importance of this lies in the fact that, when positron annihilation spectroscopy is used to probe thin layers on a substrate, different defective regions can be identified: the surface of the sample, the layer, the interface layer-substrate and the substrate. It then becomes necessary to know which region is being investigated.

## b-Diffusion

After implantation and thermalisation, the positrons diffuse through the solid and behave like charged particles. The diffusion coefficient of positron can be estimated by the following equation [42]:

$$D_+ = \frac{\mu k_b T}{e} = \frac{k_b T \tau_{rel}}{m_+} \quad (2.14)$$

$\mu$  is the mobility of positrons,  $k_b$  Boltzmann's constant,  $T$  the absolute temperature.

$e$  the charge of electron and  $m_+$  the effective positron mass.  $\tau_{rel}$  is the relaxation time for the diffusion mechanism.

The effective diffusion length for positrons can be estimated from the following relation [42],

$$L_+ = \frac{D_+^{1/2}}{(K_d n_d + \lambda_l)^{1/2}} \quad (2.15)$$

where  $\lambda_l$  is the positron annihilation rate,  $K_d$  the trapping rate and  $n_d$  the defect density.

In the case of a defect free material the positron diffusion length is expressed as:

$$L_+ = \frac{D_+^{1/2}}{(\lambda_l)^{1/2}} \quad (2.16)$$

The positron diffusion can be significantly influenced by the presence of electric field and this was experimentally verified by positron diffusion study by Corbel et al. [44] and Britton et al. [45]. The presence of structural defects and electric field influence the effective diffusion length. The effective diffusion length was found to increase with the electric field strength and this result was confirmed by Monte Carlo simulation of the positron drift under the influence of an electric field [46].

### c-Trapping and detrapping

During diffusion the positron may be trapped into a lattice defect and this constitutes the basis of different positron techniques for the detection of defects. The dominant trapping process is determined either by the diffusion of positrons to the defects or by the transition of the positron to deep bound states related to defects. The trapping rate  $\kappa_d$  is proportional to defect density  $C_d$  [47]

$$\kappa_d = \zeta C_d \quad (2.17)$$

where  $\zeta = v\sigma$  is the positron trapping coefficient which can be understood as the product of the thermal velocity  $v$  and the positron trapping cross-section  $\sigma$ .

The temperature dependence of the trapping rate of positrons is an important experimental issue as thermal fluctuations can lead to positron detrapping. The charge of the defect also influences the trapping coefficient: positively charge defects repel positrons and then the trapping rate is expected to be very small. On the other hand negatively charged defects enhance the initial positron density in defects region and increase the defects trapping coefficient.

#### **d-Annihilation of positrons.**

Annihilation occurs when a positron happens to find itself close to an electron, both particles being essentially at rest. The two particles simply disappear, converting all the energy associated with their masses, into the radiant energy of gamma rays. The number of photons arising from the annihilation process depends on the spin of the electron-positron pair and the presence of other particles or nuclei around the annihilation sites. The dominant process is the annihilation which gives rise to two oppositely oriented gamma rays, but annihilation processes with one or three gamma rays may also happen.

Under certain conditions the positron does not immediately annihilate with an electron but binds with it to form a kind of a hydrogen-like atom, positronium, where the positron has replaced the proton. Positronium occurs either in a singlet state called para-positronium or in a triplet state termed ortho-positronium. Positronium is likely to be detected at the surface of the

sample or in the vacuum because positronium which is formed in solids is much more likely to encounter an electron with the appropriate opposite spin and annihilate.

### 2-3-3 Momentum distribution techniques

The momentum techniques are based on the conservation of momentum during the annihilation process, which provides information on the electron momentum distribution at the annihilation site. Two techniques are based on the momentum distribution: angular correlation of annihilation radiation and Doppler-broadening spectroscopy. In our work only the latter one has been used and our discussion will be focussed on the Doppler-broadening techniques, particularly on the line shape parameters.

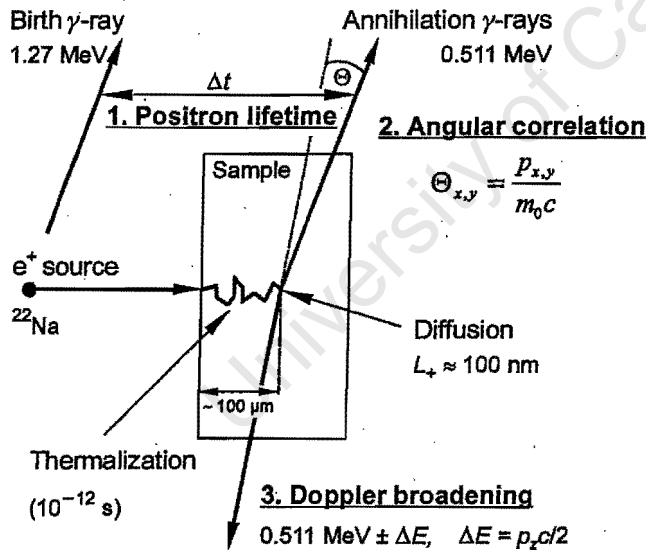


Figure 2.3: Scheme of different positron experiments [42]

### 2-3-3-1-Electron momentum spectroscopy

During the annihilation process it can be assumed that the positrons annihilate from the bulk and from possible defects and the momentum  $p$  of the annihilating particles is transferred to the photon pair.

The momentum component  $p_z$  in the propagation direction  $z$  of the  $\gamma$  quanta results in a Doppler shift  $\Delta E$  of the annihilation energy of 511 keV. Since numerous annihilation events are measured to give the complete Doppler spectrum, the energy line of the annihilation is broadened due to individual Doppler shift in both directions  $\pm z$ . Two parts of the profile are of interest: the low-momentum central part of the peak and the high-momentum tail.

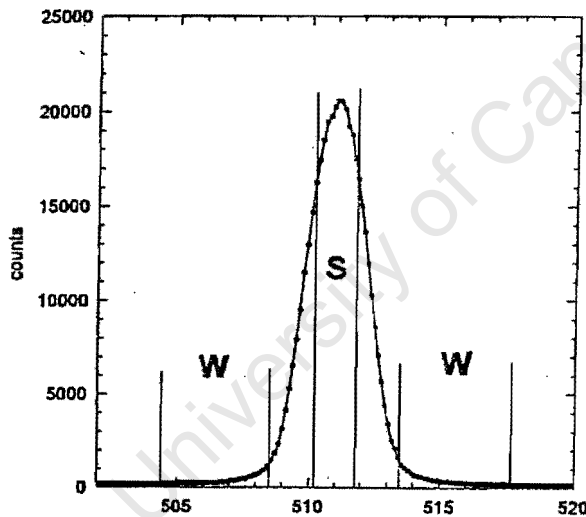


Figure 2.4: A Doppler broadened 511 keV peak measured for perfect silicon. The intervals used for defining the  $S$  and  $W$  parameters are indicated [48].

The shape of the profile can be characterised quantitatively with the aid of two parameters  $S$  and  $W$ : the  $S$  parameter (low momentum fraction) defined as the ratio of counts in a

central portion of the annihilation photo-peak to the total counts in the peak while the  $W$  parameter (high momentum fraction) is the ratio of count in the wings of the annihilation photo-peak to the total counts in the peak (fig.2.4). The interval limits of the windows used to calculate these parameters are chosen symmetrically around the energy 511 keV and are kept constant for all spectra to be compared.

Due to its positive charge, the positron is repelled by the ion cores. It therefore has the maximum probability density in the interstitial region where it annihilates mainly with low momentum electrons and contributes to the centre of the profile. A missing atom represents an attractive potential well, which may trap a positron. The absence of the atom with its core electrons manifests itself as a decrease of high momentum content and thus a sharpening of the profile.

Due to the linearity of lineshape parameter, if there are several possible modes of positron annihilation in a material with probabilities  $f_i$  and corresponding  $S$  parameter  $S_i$ , then the measured  $S$  parameter will be calculated from

$$S = \frac{\sum_i f_i S_i}{\sum_i f_i} \quad (2.18)$$

with a corresponding expression for  $W$ .

Each profile is represented by a point in the diagram of  $S$  versus  $W$ . If a number of profiles are measured under variation of some external parameter, which affects positron trapping, special points may be distinguished in the  $S$ - $W$  diagram which correspond to the situation in which all positrons annihilate via one and the same mode. This mode may be the annihilation of

free positron from the bulk of a defect free sample, or the saturation annihilation from a particular type of defect. Intermediate situations, in which there is a mixture of annihilation from defects and from the bulk, will be represented by a point on the a straight line connecting these two special points [49].

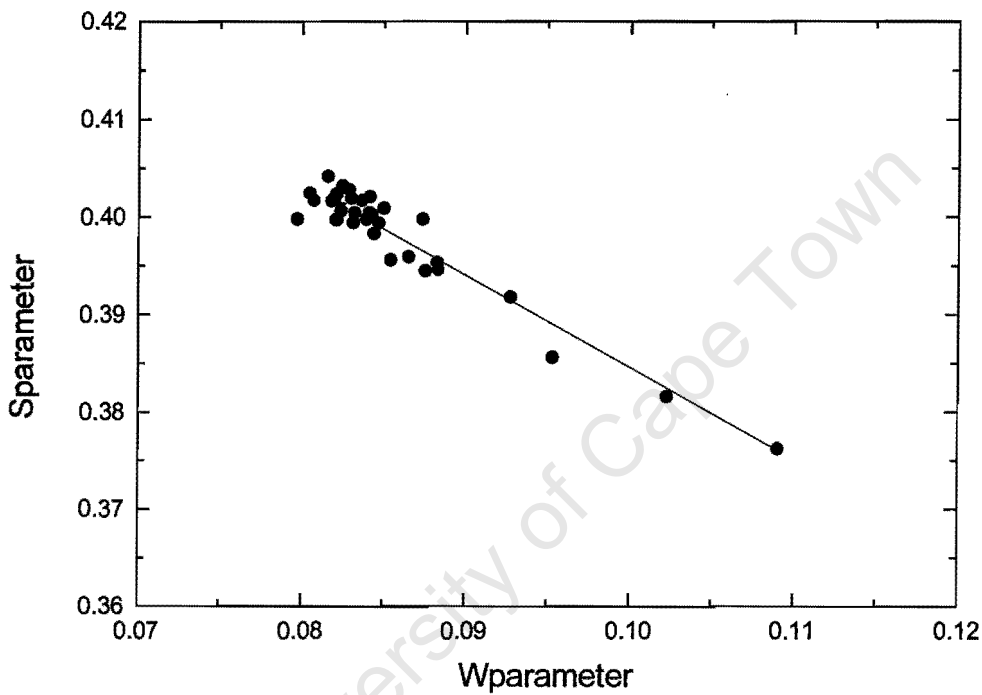


Figure 2.5: the diagram of  $S$  vs  $W$  parameter for an amorphous silicon sample deposited on a silicon substrate.

The  $S$ - $W$  map allows one to distinguish annihilation from different types of defects that on the basis of measurements of the  $S$  or  $W$  parameter would go undetected. The basic defect types detected are open volume defects such as vacancies, vacancy clusters, dislocations and grain boundaries.

## 2-4 Conclusion

In this chapter we discussed the theory behind X-ray diffraction and positron annihilation techniques. The X-ray diffraction technique in the form of the RDF was found to be a powerful method to investigate the microstructure of amorphous material as it can visualize the small differences in the structure of samples prepared almost in the same conditions. Small errors, which may occur due to the small range of the magnitude of scattering vector  $k$  compatible with the experimental arrangement, are minimized by the normalization of the scattering intensity. However, we have seen that the RDF is an one-dimensional representation of a three-dimensional system and may indeed carry a limited amount of information, thus, computational modelling is still needed as the isotropy and homogeneity in the sample may not be perfect.

It has also been shown that the positron annihilation techniques can provide information which is complementary to that provided by other techniques used for the analysis of composition and structure of materials. It was found to be a very useful method in the probe of structural defects in amorphous material. Changes in the line shape parameters are associated with the changes in the size or concentration of defects in the sample. The  $S$ - $W$  map can give an insight on the nature of defects investigated if more than one kind of defect is present in the sample.

The third chapter of this thesis will discuss the positron beam at University of Cape Town (UCT) and the X-ray diffraction machine at iThemba LABS before the presentation of the results.

## CHAPTER 3

### EXPERIMENTAL TECHNIQUES

The theoretical basis behind the two experimental techniques used to investigate the microcrystalline phases and the structure of defects in a-Si:H samples used in this work were discussed in the preceding chapter. This chapter describes how these techniques were exploited and how the measurements were conducted. This will provide a good understanding of the results and give an idea on the accuracy of our measurements.

#### 3.1 Sample characteristics and growth conditions.

As seen previously amorphous materials are produced through non-equilibrium processes and thus, opto-electronic properties of prepared samples depend upon the preparation methods and deposition parameters [1].

The a-Si:H layers on the samples under investigation were deposited by hot wire chemical vapour deposition (HWCVD) on barium borosilicate glass (Corning 7059) substrate in an atmosphere of pure silane gas ( $\text{SiH}_4$ ). Except the substrate temperature which was varied from 300 °C to 500 °C in steps of 50 °C, others conditions were kept constant during the deposition. The deposition process lasted for approximately 30 minutes for each sample under a total silane pressure of 40  $\mu\text{bar}$ .

The substrate was cleaned before the deposition by washing it in acetone and methanol. The temperature of the tantalum filament was always in the region of 1600 °C

The thickness of the grown layer was determined by profilometry and ranged between 1241 and 3367 nanometres while the bonded hydrogen concentration in the layers, estimated by the Fourier Transform Infrared Spectroscopy (FTIR), was ranging between 0.50 and 10.53 atomic per cent.

Table 3.1 summarizes the deposition parameters and the characteristics of all a-Si:H samples used in this study. It can be noted that the bonded hydrogen concentration in the layer deposited at 500 °C is quite high, but that is the information we have got from the supplier.

Serial number	Deposition temperature (°C)	Hydrogen content (at. %)	Thickness of the layer (nm)	Silane pressure [ $\mu$ bar]
Mw090	300	10.2	1980	40
Mw091	350	5.37	2383	40
Mw093	400	0.77	2288	40
Mw094	450	0.50	3367	40
Mw095	500	10.53	1241	40

*Table3.1: The growth parameters and characteristics of the a-Si:H layers used in this study.*

### **3-2 Positron beam at UCT**

The positron beam at UCT, like any positron beam set up [48], comprises the following steps: the generation of positrons and moderation, the beam transport, and the detection and collection of annihilation gamma rays resulting from the annihilation processes. These steps are discussed in the case of the UCT positron beam.

#### **a) Generation and moderation of positrons.**

As discussed in the previous chapter, positrons may result either from the  $\beta^+$  decay in the radioactive source or from the inverse of annihilation process called pair production. The choice of the source is decided according to the nature of the measurements, the cost and other advantages provided with that source, such the half life of the source and the facility to be manipulated.

The source used in the UCT positron beam is a sodium isotope in the form of sodium carbonate ( $^{22}\text{Na}_2\text{CO}_3$ ) produced locally at iThemba LABS, formerly the National accelerate centre (NAC). This source was chosen because of the increased ease and quality of deposition combined with a higher specific activity per unit volume [50]. The source is deposited in thin tantalum boat held in position by a metal retaining plug. The outer capsule has the form of smooth stainless steel cylinder of diameter 15mm with a 4 $\mu\text{m}$  pinhole free titanium window.

The positrons generated in the  $\beta^+$  decay reaction by such sources exhibit a broad energy distribution and can penetrate deep into the sample [41]. However many problems in semiconductors physics are related to thin layers and to defects near the surface and interface. These experiments required mono-energetic positrons with an adjustable energy range in order to

provide with a depth profile of defects in the material investigated. Moderators used to slow down these positrons are negative work function materials, with specific characteristics such as narrow energy width or maximum yield [43].

Various source /moderate configurations have been adopted in order to maximise the efficiency of these moderators. We can mention the back reflection geometry, the transmission geometry and the venetian blind geometry [fig.3.1].

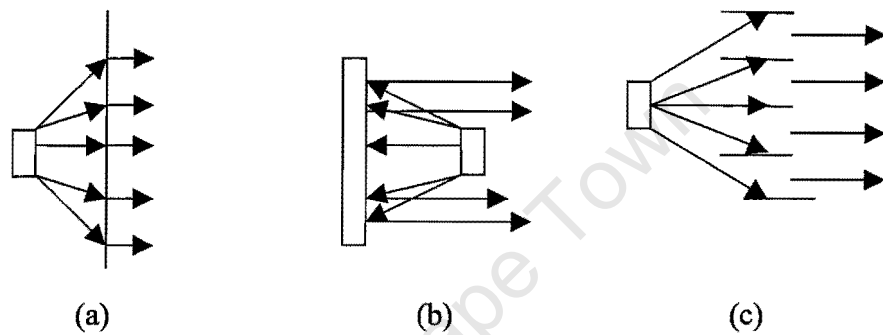


Figure 3.1: Different source/moderator configurations: (a) transmission geometry; (b) back reflection geometry; (c) Venetian blind geometry

The positron beam at UCT uses a pure tungsten grid moderator ( $1\mu\text{m}$  thick W (100) foil), which is a kind of modified venetian blind moderator and slowed positrons are extracted from the moderator by an applied potential of 200V and guided through a beam line to the sample chamber.

Figure 3.2 shows a diagram of UCT positron beam

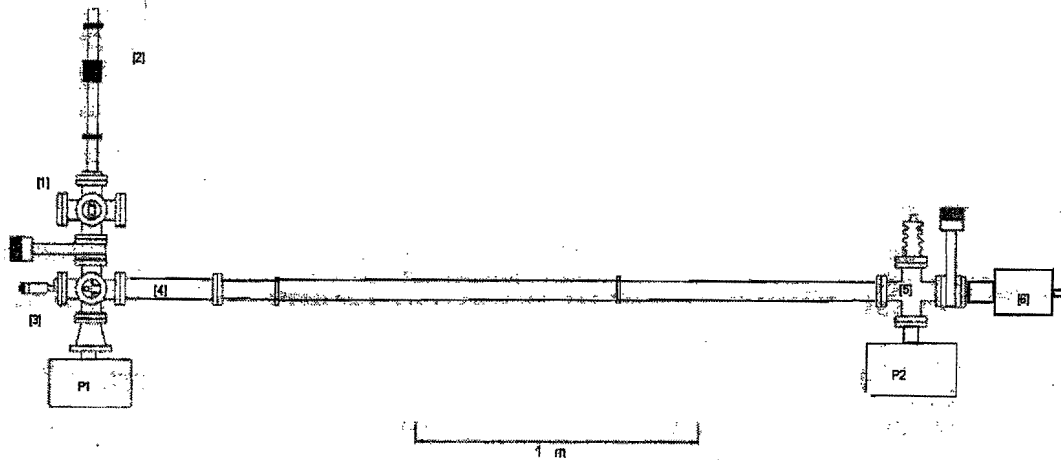


Figure 3.2: Diagram of the positron beam at the University of Cape Town: (1) moderator preparation chamber; (2) linear transport on which the moderator is mounted; (3) source chamber; (4) magnetic deflector and the beam stop; (5) five elements accelerator; (6) sample chamber; P1 and P2 are ion getter pumps

### b) Beam transport

Once the slow positrons, moderated to a mono-energetic beam, have been extracted from a moderator, they are guided through a vacuum system to the sample using various methods depend on the given experiment. We can mention purely electrostatic or magnetic systems or a hybrid positron beam transport system. The fundamental difference between those systems is basically that some experiments require the measurement of scattering angles, which is hidden by magnetic system while others need to confine all scattered charged particles.

The system used at UCT is purely magnetic field system where the positrons are guided through a 2,5 m long beam line. The magnetic field  $B$  of a value of 20.4 mT, for a used current of

6.5 A, is produced by a solenoid wound onto a 70 mm diameter outer tube. A 15 mm inner tube diameter is maintained at a potential corresponding to the final beam energy. The outer tube is maintained at zero potential. Positrons are confined by gyration motion around the axial field provided from the solenoid and the radius  $R$  of the spiral path of a positron is given by:

$$R = \frac{m_e v}{eB} \quad (3.1)$$

where  $B$  is the magnetic field,  $m_e$  the mass of a positron and  $v$  the transverse velocity.

Unmoderated positrons are prevented from entering the beam line by a purely magnetic deflector system which deflects the low energy beam off axis along the bent inner tube and a second one which brings it back onto axis.

### **c) Detection of the annihilation gamma rays.**

After being accelerated to the desired incident energy, positrons are guided to the sample where they annihilate with electrons of surrounding atoms. The stopping profile depends on the nature of the sample and the final beam energy.

UCT's positron beam uses a pure germanium coaxial detector to measure the Doppler broadening of the 511KeV gamma line from annihilation in the sample. The detector, which is basically a diode with a very thick junction, has liquid nitrogen as cooling system. The annihilation gamma rays produce electron-holes pairs which are collected as charges pulse and are pre-amplified before they are sent the main amplifier and finally to a PC equipped with a multi-channel analyser card (MCA). The height of the final pulse is proportional to the number of electron-holes pairs and therefore to the energy of the gamma rays. The MCA comprises an analogue-to-digital converter (ADC), which converts the analogue information contained in each pulse into digital form suitable for storage in a memory, and the content of the MCA memory

can be displayed visually as counts versus channel number, where the channel number corresponds to the energy. These data collected form a Doppler spectrum which provide information around the annihilation sites.

### 3-3 X-ray phase analysis diffractometer at iThemba LABS

Any X-ray diffractometer comprises an X-ray tube, a system of slits which define and collimate the incident and diffracted beams and a detector. These elements are discussed in the case of the D8 advanced theta-two-theta diffractometer from Bruker analytical X-ray systems used in our measurements at iThemba LABS, and figure 3.3 below shows a picture of that machine.

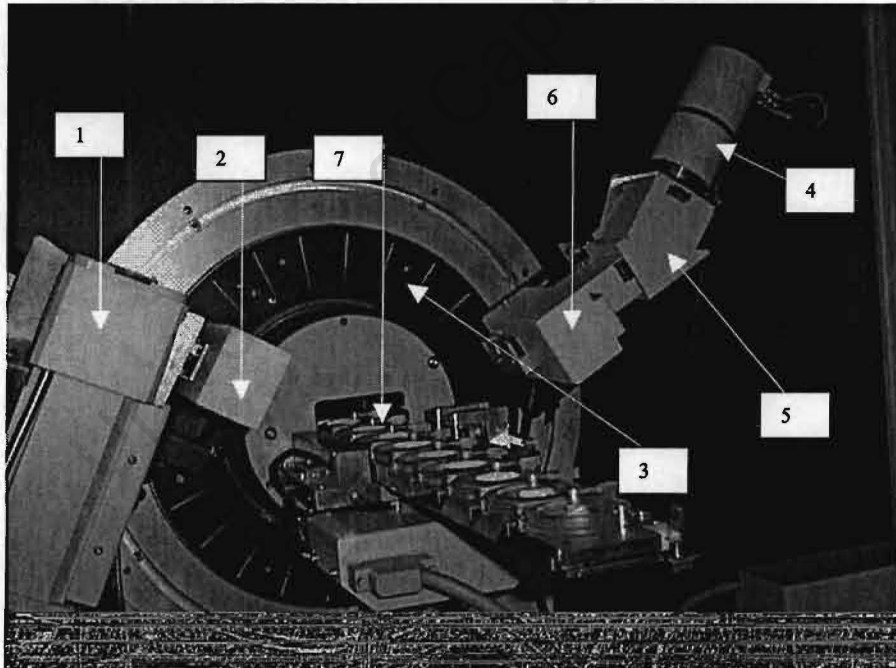


*Figure 3.3: X-ray phase analysis diffractometer: 1 - X-ray tube, 2 - divergence slit, 3 - vertically oriented goniometer, 4 - detector, 5 - monochromator, 6 - antiscatter slit, 7 - automatic sample magazine*

The primary side of the diffractometer comprises the X-ray tube (1) which provides an incident monochromatic  $\text{CuK}\alpha$  X-ray radiation. However, that beam is quite divergent and a variable divergence slit (2) is placed in front of the tube and helps to define and collimate the incident X-ray beam. The incident X-ray beam, inclined under an  $\theta$  angle, strikes the sample in reflection mode and the diffracted radiation from the sample, scattered through a  $2\theta$  angle, is then further directed toward the detector in the secondary side.

A system of slits, which are placed in front of the detector helps to define and collimate the diffracted X-ray beam. These slits are an antiscatter slit (6) and a detector slit. In addition to that a monochromating system (5), which is set to diffract only  $\text{K}\alpha$  radiation, is added and helps to filter the unwanted  $\text{K}\beta$  radiation from the diffracted beam in order to keep a selected single wavelength beam but has also another advantage of suppressing the background radiation originating in the specimen such as fluorescent radiations or incoherent scattered radiations.

The sample holder (7), which is an automatic sample magazine with nine sample slots, is placed into the centre of the goniometer (3) and the sample can rotate about an axis within the horizontal plane.

The scattered x-rays radiations can be detected by means of the scintillation counters. The counters which depend on the power of X-ray to ionise atoms of solid in the case of scintillation, are interesting in terms of counting losses, efficiency and energy resolution. The efficiency of scintillation counters approaches 100 percent over the usual range of wavelengths [38]

The counter and the receiving slits are supported on a carriage, which is power-driven at a constant angular velocity, through increasing values of  $2\theta$  until the whole angular range is scanned and the diffracted X-ray radiation detected by the detector are converted into electric pulses, which are processed by a multichannel analyser (MCA) as mentioned in section 3.2.

The scattered intensity is measured as a function of  $2\theta$ , which can be converted into wave vector  $k$  as defined by equation (1.2). It can be noted that the axis of the diffractometer is horizontal and the detector and the X-ray tube can only move in vertical plane. The upper angular limit of X-ray tube-counter motion is determined by contact between counter and X-ray tube.

### 3-4 Measurements

A set of five a-Si:H samples were investigated using both techniques describe above.

The experimental arrangement employed in X-ray phase analysis measurements is schematically shown below (fig3.4).

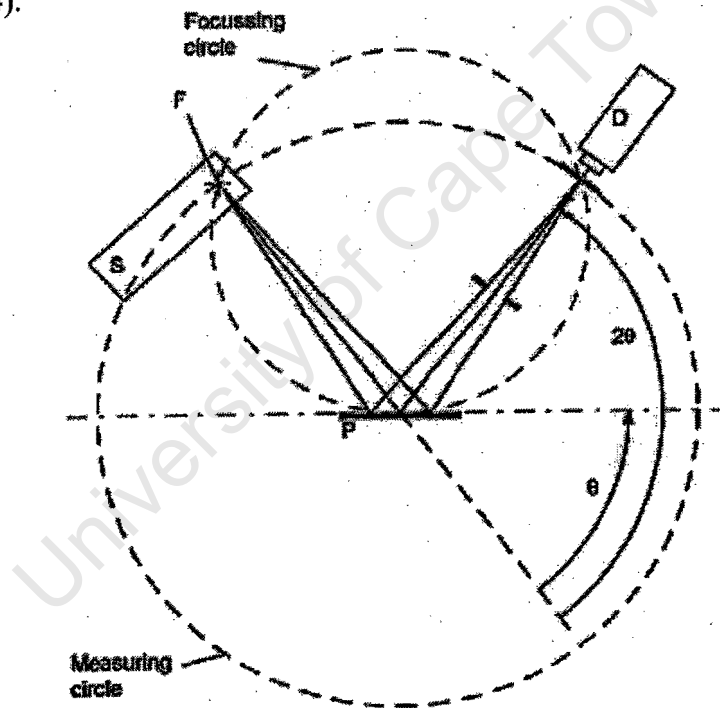


Figure 3.4: Schematic diagram of the experimental configuration for X-ray phase analysis measurements:  $\theta$  -Incidence angle;  $2\theta$  -Diffraction angle; R- X-ray tube, AB-divergence slit, P-sample, SB- antiscatter slit,  $K_{\beta}$  - monochromating system; DB - detector slit and D – the detector.

The measurements were performed in Bragg-Brentano geometry, using a  $\text{CuK}\alpha$  radiation from a Cu tube operating at 40 kV and 40 mA. To strictly match the Bragg-Brentano geometry, the sample needs to be curved according to the focussing circle in order to allow the scattered beam to focus at the detector. This was not the case in our experiments but this condition was fulfilled by keeping the surface of the sample tangent to the focussing circle. The diffraction patterns were recorded over a  $2\theta$  range between  $10^\circ$  and  $70^\circ$  with a step size of  $0.04^\circ$  and a minimum measuring time of 60 sec per step. The sample was rotated permanently within the horizontal plane to allow all planes of atoms to be investigated in the same conditions and the measured intensity was an average from different planes. A polystyrene sample holder was used to eliminate any spurious crystalline peaks from the spectrum.

X-rays can penetrate deep in thin layers and may reach the substrate. The diffracted intensity in this case is made up of contributions from the layer below the surface and also contribution from the substrate and the sample holder can be expected. The effect of the substrate was then removed by measuring the reverse side of the sample and subtracting it from the front side signal. After stripping the substrate and the sample holder pattern from the data, the pattern was smoothed by adjacent averaging. The radial distribution function was then calculated by the numerical sine transform of the scattering factor as a function of scattering vector  $k$ .

Positron measurements in the form of lineshape parameters were carried out using the continuous positron beam at the University of Cape Town as described in section 3.2. The incident positron energy was continuously varied up to the maximum of 16 keV with a step size of 0.3 keV below the energy of 6 keV as the changes in the line shape parameters are significant

in that region and an increase step of 0.6 keV was adopted beyond that region where those line parameters do not fluctuate a lot. The measuring time was 30 minutes per step and around 35 steps were required to complete the measurements on one sample. A window of a 100 channels was chosen in the annihilation peak and, in order to get the maximum information around the annihilation site, windows, around the peak position, within which the low momentum fraction was calculated was chosen to get  $S$  values close to 0.5 while the high momentum fraction  $W$  was estimated far away in the wings.

The mean penetration depth, estimated according to equation (2.13), was increased up to 1.6  $\mu\text{m}$  with a standard deviation of about 0.8  $\mu\text{m}$ . Considering the thickness of the layers under investigation [table 3.1], the penetration depth was sufficient for our investigations as the separation between a-Si:H layers and substrate contribution was to be taken into account.

### 3-5 Conclusion

In this chapter we discussed the positron beam at UCT and X-ray diffraction machine used to investigate our samples and how the measurements were conducted. The interpretation of these results will give us information around the annihilation sites provided by the annihilation lineshape parameters and information about the short range order, and hence the nature of chemical bonding, provided by radial distribution function. Thus, the structure of atoms in the material can be extracted from these measurements. The good quality of the equipment used to perform these experiments and precautions taken during those measurements predict an unambiguous accuracy. The next chapter presents these results in the form of the radial distribution function and Doppler broadening line shape parameters from different samples under investigation.

# CHAPTER 4

## RESULTS

Results from different measurements performed on the a-Si:H samples under investigation are presented separately according to the technique used to collect them: Electron momentum fractions  $S$  and  $W$  are plotted as function of the depth penetration for positron measurements while X-ray diffraction patterns and the RDF were adopted for X-ray diffraction measurements.

### 4.1 X-ray diffraction results

As can be seen on the figure 4.1 below, which shows the X-ray diffraction pattern of the sample MWO94, the X-ray diffraction measurements performed on our samples yield only diffuse peaks, indicating thereby that all the layers under investigation are amorphous.

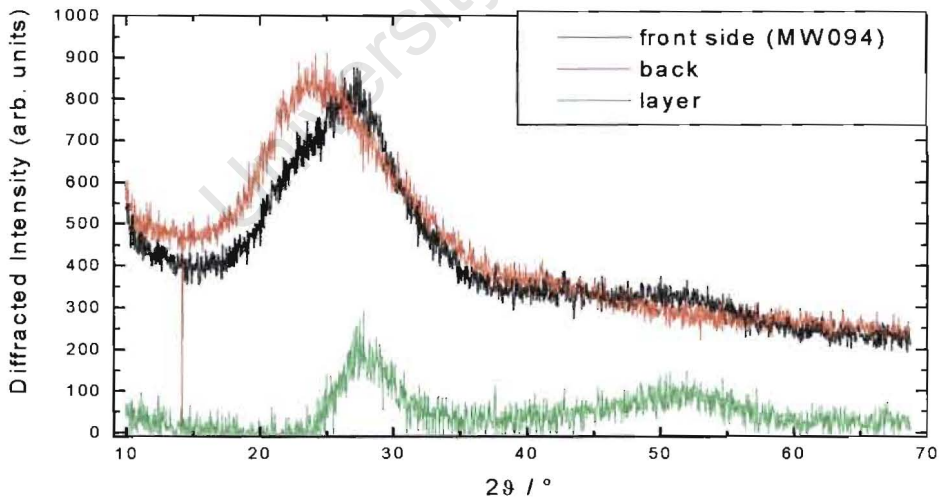


*Figure 4.1: X-ray diffraction pattern for a 2288 nm thick a-Si:H layer deposited on glass substrate at a substrate temperature of 400 °C.*

Figure 4.2 shows the radial distribution densities of the five samples used in this study. The first peak, corresponding to the nearest neighbour separation, is poorly resolved, only appearing as a shoulder in some cases. This was associated to the limited range of scattering vector  $k$  accessible to the experiment as discussed previously in chapter 2. The maximum  $k$  value, in the case of the  $\text{CuK}\alpha$  radiation used in our experiments ( $\lambda=1.54 \text{ \AA}$ ), is only  $5 \text{ \AA}^{-1}$  for the maximum scattering angle of  $70^\circ$  while a perfect real space transform required an infinite range of  $k$  values as discussed in section 2.2. This leads to a limit on the spatial resolution of approximately  $0.6 \text{ \AA}$ .

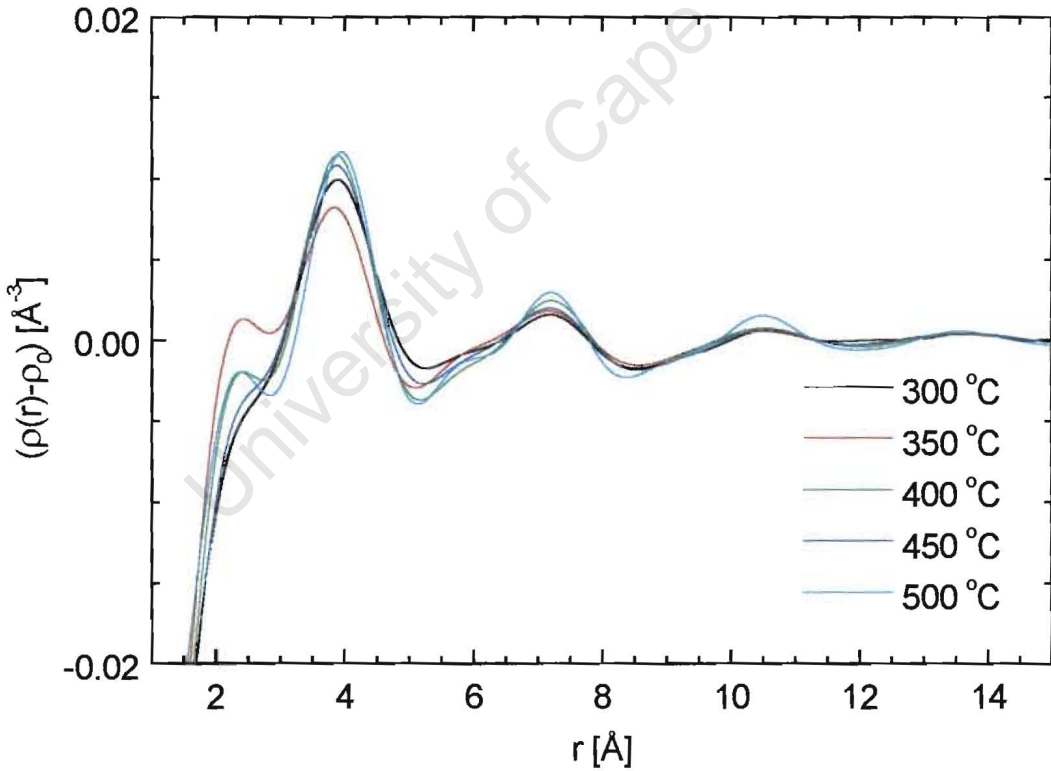


Figure 4.2: The radial distribution function for  $a\text{-Si:H}$  layers grown by HWCVD at different deposition temperatures ranging from  $300 \text{ }^\circ\text{C}$  to  $500 \text{ }^\circ\text{C}$ .

It can be seen from figure 4.2 that, with the exception of the layer grown at 350 °C, the peaks in the RDF become more pronounced with increasing growth temperature. There is also a general decrease in nearest neighbour distance, and an increase in second nearest neighbour separation with growth temperature. These are both indication of a widening of the average bond angle and a shortening of its length. Quantitative estimates for those parameters, taken from the peak position in the figure 4.2 are listed in the table 4.1 below.

For different deposition temperatures between 300 °C and 500 °C the mean bond length decreases by 2.5% from  $2.36 \pm 0.01$  Å to  $2.30 \pm 0.01$  Å and the average bond angle increases from  $111 \pm 0.9^\circ$  to  $119.3 \pm 1.1^\circ$

Deposition temperature $T$ [°C]	Thickness of the sample $d$ [nm]	Hydrogen content $H$ [at. %]	Bond length $R$ [Å]	Bond angle $\alpha$ [°]
300	1980	10.2	$2.36 \pm 0.01$	$111.0 \pm 0.9$
350	2383	5.37	$2.33 \pm 0.01$	$111.4 \pm 0.9$
400	2288	0.77	$2.33 \pm 0.01$	$113.2 \pm 1.0$
450	3367	0.5	$2.31 \pm 0.01$	$114.7 \pm 1.0$
500	1241	10.53	$2.30 \pm 0.01$	$119.3 \pm 1.1$

*Table 4.1: Characterisation of the a-Si:H layers grown by HWCVD on glass substrate at different temperatures, the thickness of the sample  $d$  was estimated by profilometry while the total hydrogen content  $H$  was determined by FTIR. The bond length  $R$  and the bond angle  $\alpha$  were estimated from the RDF (fig.4.2)*

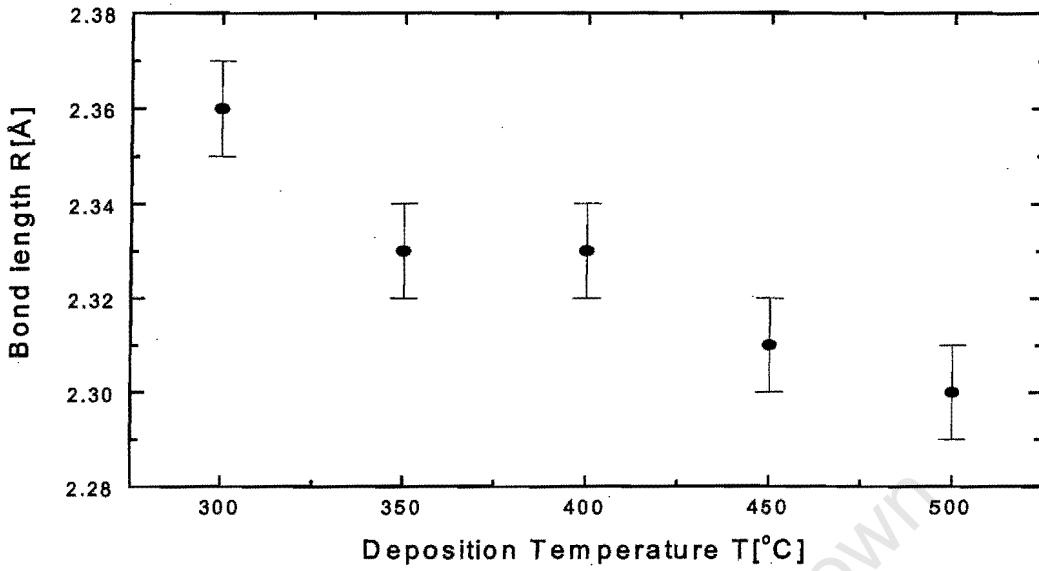


Figure 4.3: Dependence of the nearest neighbour separation  $R$  on the deposition temperature for all  $a\text{-Si:H}$  layers grown by HWCVD at different glass substrate temperatures

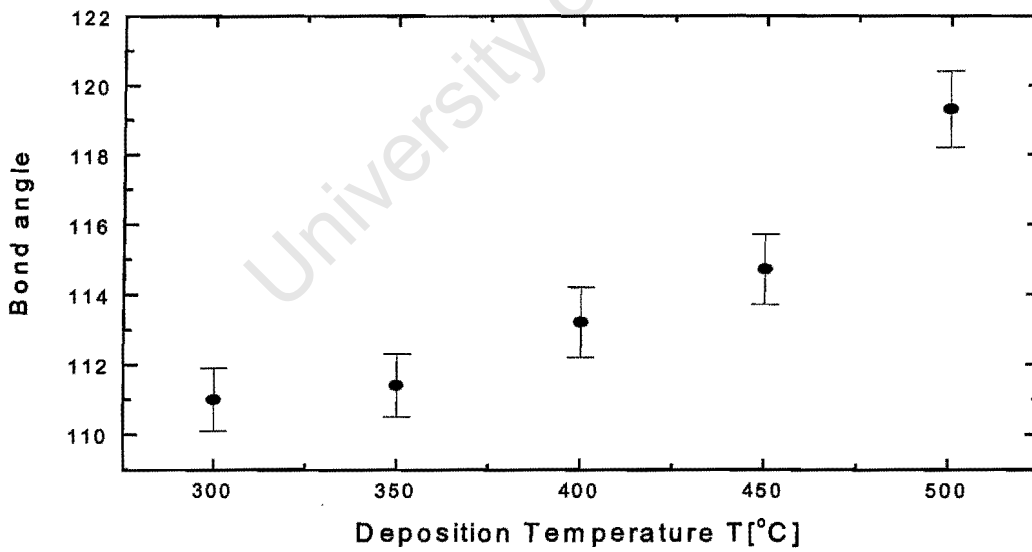


Figure 4.4: Dependence of the bond angle on deposition temperatures for the  $a\text{-Si:H}$  layers deposited by HWCVD on glass substrate at different temperatures

## 4.2 Electron momentum spectroscopy.

The electron momentum fractions  $S$  and  $W$  of the annihilation line shape are presented as a function of the mean penetration depth, measured in nanometres, for the sample *MW094* deposited on glass substrate at 450 °C and hydrogen content of 0.5 atomic per cent. This was motivated by the fact that all layers under investigation were found to be uniform.

The penetration depth, which is a function of the incident positron energy [eq. 2.13], has been calculated assuming the density of silicon to be 2.30 g.cm<sup>-3</sup>. This value of the density provides good agreement between all Doppler broadening measurements and the optically determined layer thickness, and is only marginally less than that of crystalline silicon [51].

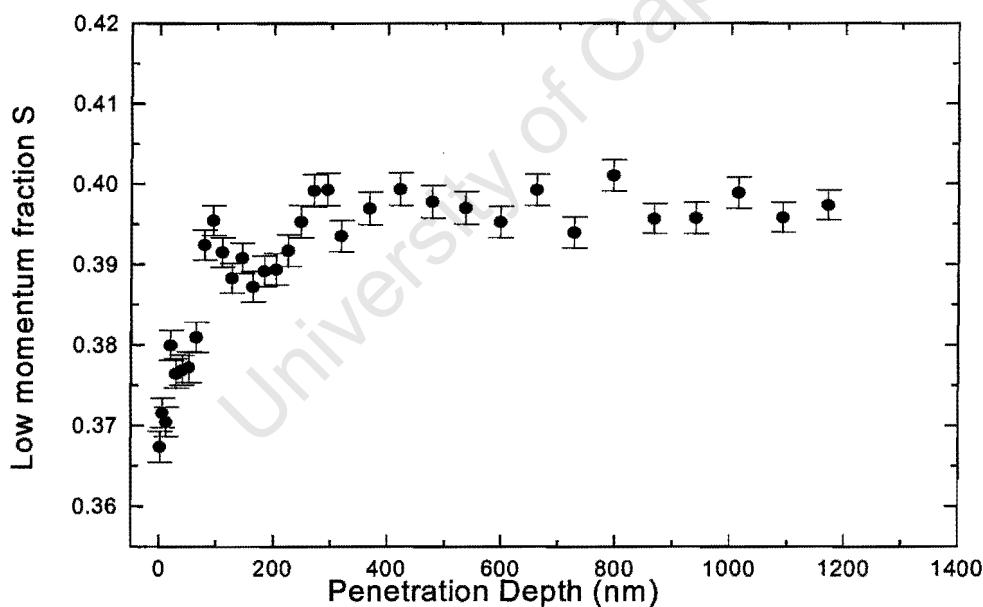


Figure 4.5: Positron line shape parameter  $S$  measured as a function of the mean penetration depth for a 3367 nm *a*-Si:H layer deposited on glass substrate at 450 °C.

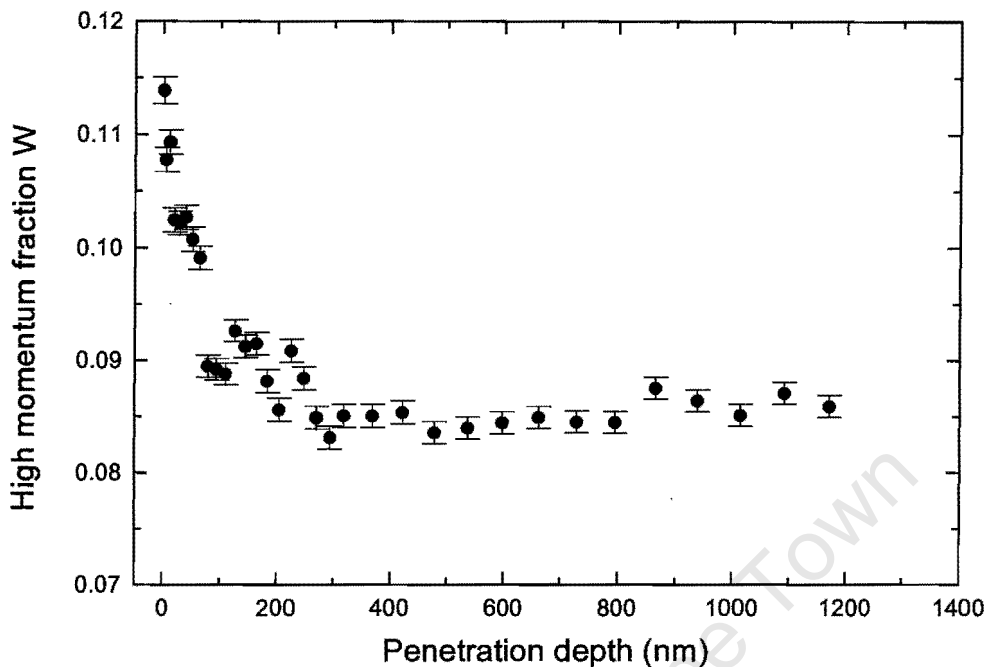


Figure 4.6: Doppler broadening parameter  $W$  as a function of the mean depth penetration for a 3357 nm thick  $a$ -Si:H layer deposited by HWCVD on glass substrate at 450 °C

Both curves have the same form with a steep increase in  $S$  parameter (a steep decrease in the  $W$  parameter) up to a stopping depth of about 200 nm followed by a constant value corresponding to the annihilation in the layer, except that the direction of the two curves are complementary.

If the two parameters are plotted against each other, a simple linear relationship should be expected and has been confirmed (fig. 4.7).

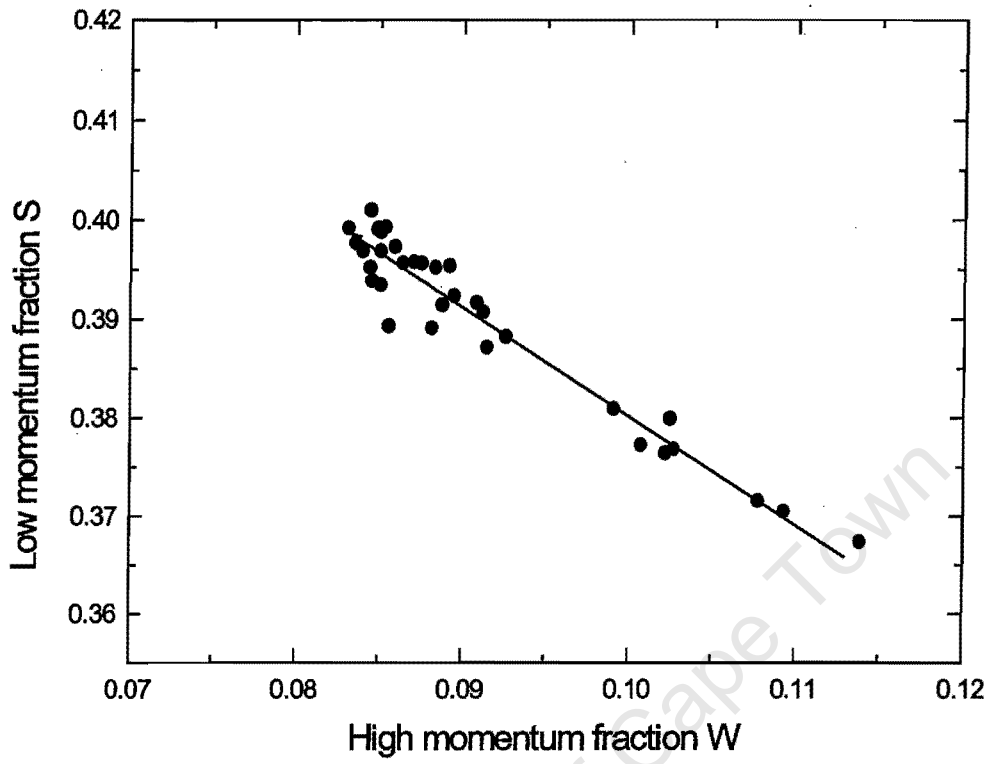


Figure 4.7: The S-W map for the 3357 nm thick  $\alpha$ -Si:H layer deposited by HWCVD on glass substrate at 450 °C

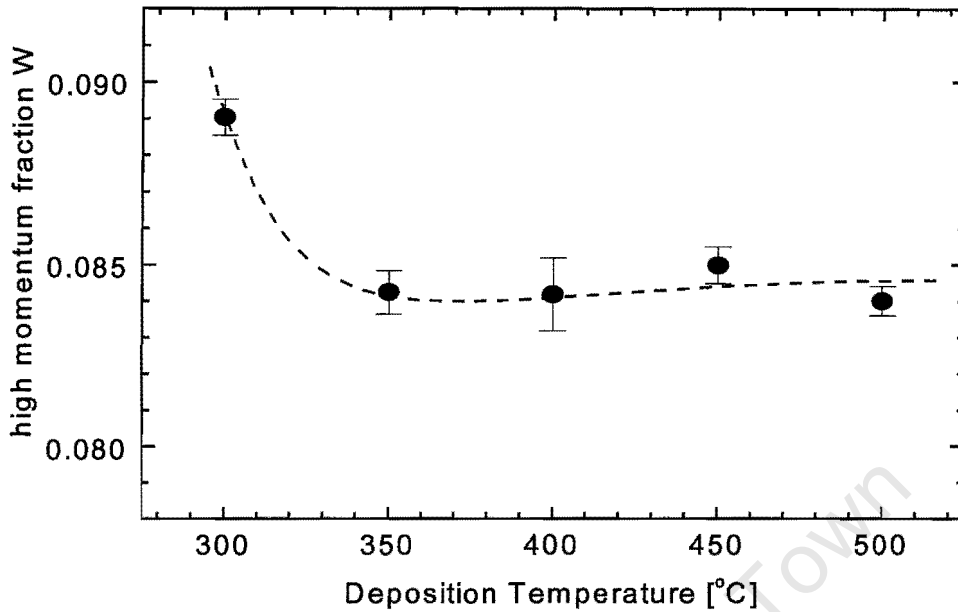


Figure 4.9: Dependence of the high momentum fraction  $W$  on growth temperature for different  $a$ -Si:H layers deposited by HWCVD on glass substrates.

### 4.3 Conclusion

In this chapter, results from different measurements are summarized. The almost complete lack of periodicity and the tendency to order, which can be seen in all the layers, result in an X-ray scattering curve showing diffuse peaks and this indicates clearly that the samples under investigation were really amorphous. The dependence of the low and high momentum fractions on the deposition temperature shows an increase in  $S$  (a decrease in  $W$ ) followed by a monotonic decrease for 50° increase in growth temperature. The RDF provides us a crucial information about the short range order: the mean bond length is seen to decrease by 2.5% while the bond angle seems to increase by increasing the substrate temperature. These results are discussed in the next chapter.

# CHAPTER 5

## DISCUSSION

The present chapter details the interpretation of the experimental data in relation to the theoretical prediction of defects structure and microcrystalline phases in a-Si:H samples deposited by HWCVD on glass substrate at different temperatures ranging between 300 °C and 500 °C under otherwise identical conditions. The results of chapter 4 are used in this discussion.

The X-ray diffractions patterns from these samples show only diffuse peaks. The first peak at a scattering angle of  $28^\circ$  correspond to the (111) diffraction peak for crystalline silicon but this peak is wider compared to measured peaks for layers with no detectable crystallinity in references [52] and [53]. This indicates that in the layers investigated there was no detectable crystalline contribution.

The reduction of defect free volume for higher growth temperatures (higher than 300 °C ) shown by a decrease in low momentum fraction and an increase in high momentum fraction (figs 4.8 and 4.9) is consistent with the increased ordering seen by X-ray diffraction, as well as the reduction in the bond length shown in figure 4.3. This variation is approximately linear with deposition temperature, indicating a continual relaxation of the network, and is tracked at higher growth temperature by the positron annihilation parameters, as can be seen in the figure 5.1 but also if we took into account that the normal c-Si bond lengths are 2.35 Å but the disilane molecule's Si-Si bond length is 2.31 Å [33].

In this range the positrons almost exclusively sample vacancy-like dangling bond defects. The reduction in the low momentum fraction with the deposition temperature is indicative of a reduction in average size of this defect, allowing more annihilation with high momentum electron, resulting from the increased order and a shortening of the bond length.

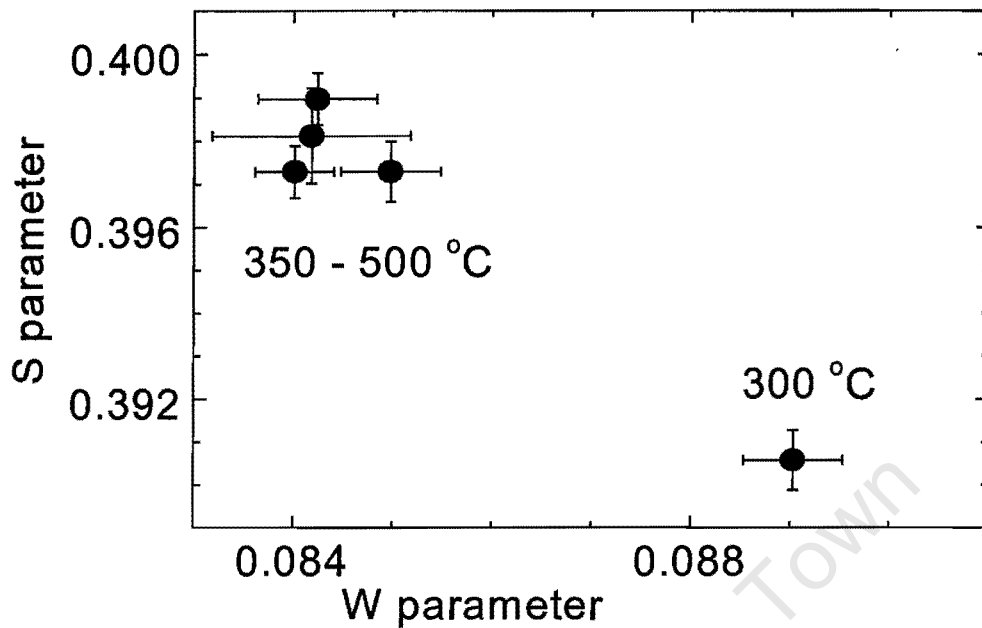


Figure 5.1: Correlation between low momentum fraction  $S$  and high momentum  $W$  for all  $a$ -Si:H layers deposited by HWCVD on glass substrate at different temperature between  $300^{\circ}\text{C}$  -  $500^{\circ}\text{C}$ .

It could therefore be supposed that the very low value of  $S$  for the layer grown at  $300^{\circ}\text{C}$  can be attributed to an even higher degree of ordering and a smaller, or few defects. This, however, is not seen in either the radial distribution density or the dependence of the nearest neighbour separation. At the lowest deposition temperature, the layer has the least order and the longest average bond length. Furthermore, from figure 4.3 the bond length appears to agree with the natural sequence of the other samples grown at higher temperature. We therefore can conclude that the reduced low electron momentum fraction for  $300^{\circ}\text{C}$  growth results from an increased defect size or concentration. For this to be the case, there must be a change in the nature of the dominant defect, and not just its size, as the growth temperature is increased above

300 °C - 350 °C. This supposition is born out by the combined behaviour of the two positron annihilation fractions as shown in figure 5.1 and the relation of bond length to low momentum fraction (fig.5.2).

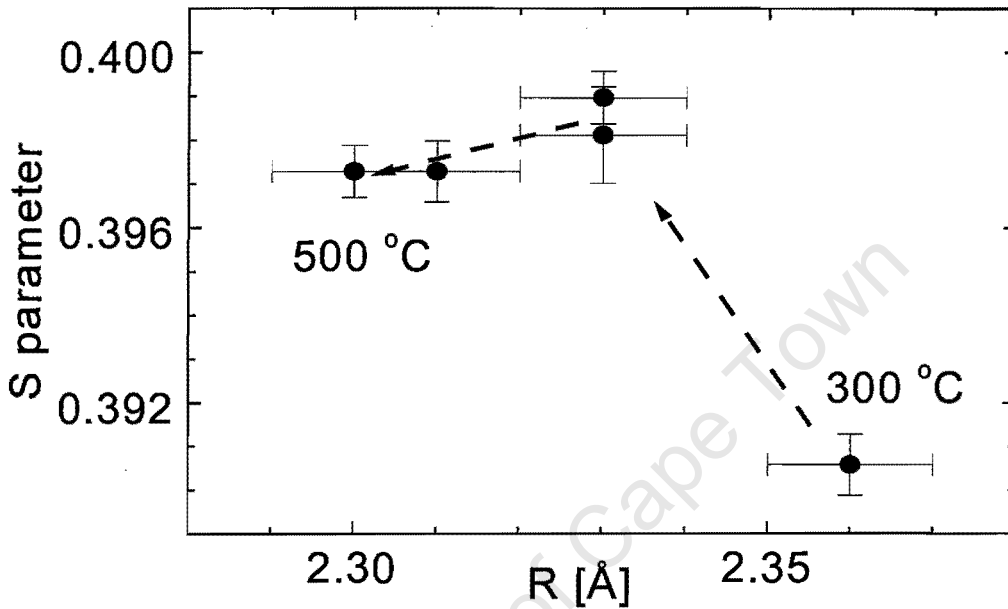


Figure 5.2: Correlation between the nearest neighbour separation  $R$  and low momentum fraction  $S$  for all samples used in this study.

With the exception of the layer grown at 300 °C, all the point cluster in the same region of the graph. This suggests that for high temperature growth, there are no qualitative differences in the defect structure, only a relaxation of its size. For low temperature growth the defects structure is fundamentally different. A possible explanation is given by the hydrogen content (table3.1), which decreases rapidly with growth temperature between 300 °C and 400 °C. It is likely that the material grown at low temperature contains large microvoids which are decorated with hydrogen. The effect of this is to mask the defect signal, by reducing the effective free volume seen by positron.

## CHAPTER 6

### GENERAL CONCLUSION

Hydrogenated amorphous silicon, as a promising material in solar cell manufacturing, is, metastable and photodegrades after a moderate light illumination because of light induced defects. These defects, which are basically dangling bonds defects, reduce its performance as most of the opto-electronic properties of that material are defect controlled. The inclusion of small volume fraction of microcrystallites was found previously to act against light defects creation and a stable material can be achieved at the edge of crystallinity with microcrystalline inclusions [35,36]

In this work, we were concerned with the study of microstructural differences in hydrogenated amorphous silicon samples deposited by HWCVD on glass substrate at different temperature, under otherwise identical conditions. Attention was also focussed on structural changes of defects in these samples in order to correlate them with the degree of crystallinity.

We have used a combined study of X-ray diffraction and positron annihilation spectroscopy to investigate these microstructural changes in the initial state of these samples. Both techniques have the advantage of being non-destructive and sensitive enough at an atomic scale as pointed out in chapter 2. Direct X-ray diffraction patterns, consisting in diffuse peaks, proved the samples to be perfect amorphous silicon and no evidence of nanocrystalline inclusions seen in the material.

The RDF, which provides information on the degree of order in the material, and the Doppler broadening line shape parameters, which provides information on the structure of defects, indicate both a relaxation of the network with increasing growth temperature, leading to a higher degree of ordering, shorter bond lengths, and a reduction in the average size of defect in the material. The bond length was seen to decrease by 2.5% from  $2.36 \pm 0.01 \text{ \AA}$  to  $2.30 \pm 0.01 \text{ \AA}$  for an increase in deposition temperature of  $50 \text{ }^\circ\text{C}$  and the bond angle to increase from  $111 \pm 0.9^\circ$  to  $119.3 \pm 1.1^\circ$  for the same increase in temperature.

For low temperature ( $300 \text{ }^\circ\text{C}$ ) growth, the layers are seen to be the most disordered, and highly defective. The dominant defects are probably microvoids, decorated with hydrogen, in contrast to the smaller dangling bond defects seen in high temperature growth.

Further work may concentrate on the study of the formation of microcrystalline phases in these samples upon annealing at different temperature as the nanocrystals inclusions were seen to grow by annealing the samples. The evolution of defects should be monitored as well during that process and correlated them to the degree of order in these samples.

## REFERENCES

- 1 A. Madan and M.P. Shaw, *the Physics and applications of amorphous semiconductors*, Academic Press, San Diego, 1988.
2. K. Morigaki, *Physics of amorphous semiconductors*, Imperial College Press, London, 1999.
3. S.R. Elliott, *Physics of amorphous materials*, 2<sup>nd</sup> edition, Longman, UK, 1990.
4. R. Mosserei, C. Sella, and J. Dixmier, *Phys. Stat. Solid* 52, (1979), 475
- 5 S.C. Moss and J.F. Graczyk, *Phys. Rev. Lett.* 23 (1969), 116
6. J.F.Sadoc, and J. Dixmier, *Mat. Sci. Eng.* 23(1976), 187.
7. H.P Klug and L.E. Alexander, *X-ray diffraction procedures for polycrystalline and amorphous materials*, 2<sup>nd</sup> edition, 1978.
8. D.E. Polk, *J. Non-cryst. sol.*, 5 (1971) 365-376.
9. Grigorovici, and R. Manaila, *J. Non-cryst. Solid.* 1 (1969), 371.
10. D.T. Britton, A. Hampel, M. Härting, G. Korgel, P. Sperr, W. Triftshäuser, C. Arendse, and D. Knoesen, *Phys. Rev. B* 64 (2001), 075403.
11. R. Bellissent, A. Meunelle, W.S., Howells, A.C. Wright, T.M. Brunier, R.N. Sinclair, and F. Jansen, *Physica B* 156&157 (1989), 217.
12. G. Lucovsky, Nemanich, R.J. and J.C. Knights, *Phys. Rev. B* 19 (1979), 2064.
13. S. Yamasaki, H. Okushi, A. Matsuda, K. Tanaka, and J. Isoya, *Phys. Rev. Lett.*, 65 (1990), 756.
14. P. O'Conner and J. Tauc, *Phys. Rev.*, B25 (1982), 2748.
15. W.B. Jackson and N.M. Amer, *Phys. Rev.*, B25 (1982), 5559.
16. D. Adler, and E.J. Yoffa, *Phys. Rev. Lett.* 36 (1976), 1197.

17. H.Yokomoshi, and K. Morigaki, Solid State Commun. 85(1987),629
18. P.G. LeComber, and W.E.Spear, Philos. Mag. B53(1986),L1
19. M. Stutzmann, W.B. Jackson, and C.C. Tsai, Phys. Rev. B32 (1985),23
20. Y. Hishikawa, K.Watanabe, S.Tsunda, S.Nakano, M.Ohnishi, and Y. Kuwano, J. Non-Cryst. Solids, 97&98(1987), 399.
21. D. Weaire and M.F.Thorpe, Phys. Rev., B4 (19971), 2508.
22. J. Singh, Phys. Rev, B, 23, (1981), 4156.
23. T. Tiedje, in Semiconductors and Semimetals, vol21, Part C, ed.J.I. Pankove (Academic Press, Orlando),(1984) p.207.
24. K. Winer, I. Hirabayashi, and L. Ley, Phys. Rev B, 38 (1988a), 7680.
25. K. Winer, I. Hirabayashi, and L. Ley, Phys. Rev. Lett. 60, (1988), 2697.
26. D. L. Staebler and C.R.Wronski, Appl. Phys. Lett.31, (1977), 292.
27. G.D.Cody,T.Tiedje, B.Abeles, B.Brooks, and Y.Goldstein, Phys.Rev.Lett .47 (1981),1480
28. D.Han, C. Qui and W, Wu, Phil. Mag. B54 (1986), L9.
29. K. Shimakawa, S. Imai, and S.R. Elliott, Phys. Rev. B42 (1990), 11857.
30. H. Oheda,J. Appl.Phys.52(1981), 6693.
31. C.H. Henry, J. Appl. Phys. 51(1980), 4494.
- 32 M.A. Green, Physica E14(2002),65
33. H.M. Branz, Private communication
- 34 I. Shimizu, J. Non-cryst.Solids.77-78 (1985),1363.
35. D.V.Tsu, B.S. Chao, S.R. Ovshinsky, S. Guha, and J. Yang, Appl. Phys.Lett.71 (1999), 1317.
36. J.Yang, A Barnerjee, and S.Guha, Appl. Phys.Lett.70 (1997), 2975.

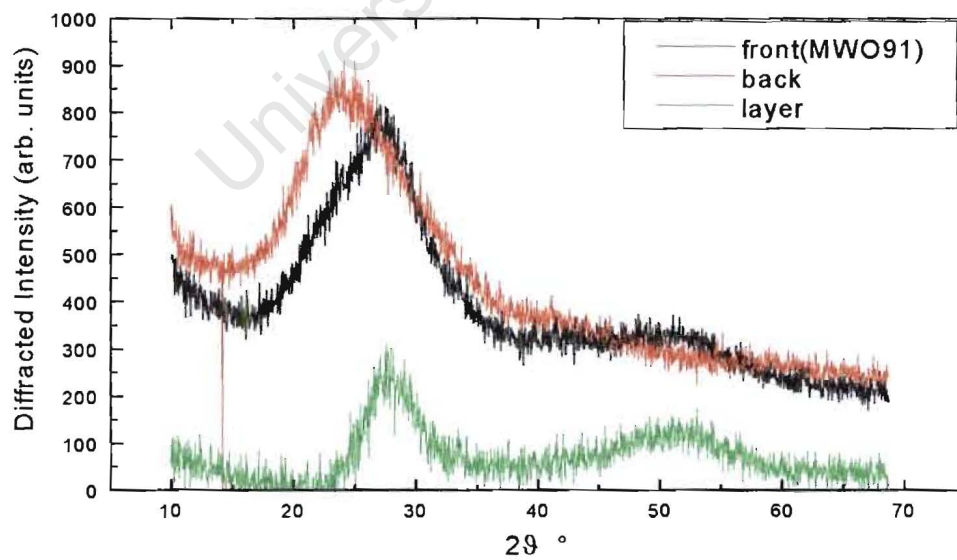
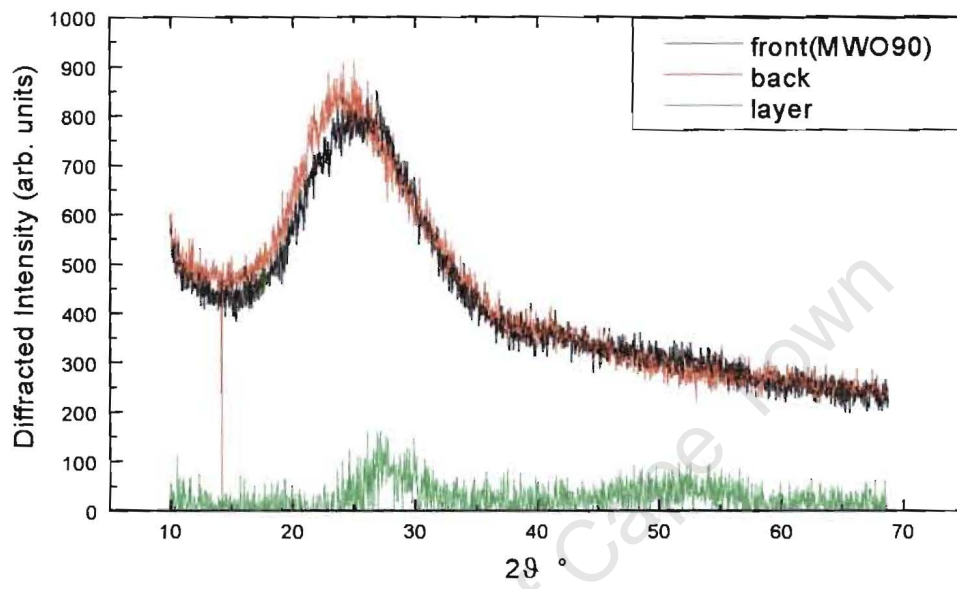
37. S. Dannefaer, D. Kerr, and B.G. Hogg, *J. Appl. Phys.* 54,(1983), 155.
38. B.D. Cullity, *Element of X-ray diffraction*, Addison-Wesley, London, 1978.
39. K.Laaziri, S. Kycia, S. Roorda, M. Chicione, J.L. Robertson, J. Wang and S.C. Moss, *Phys. Rev. B*60 (1999), 1352.
40. A. Guinier, *X-ray diffraction in crystals, imperfect crystals and amorphous bodies*, Dunod, Paris, 1956
41. P.J. Schultz, K.G. Lynn, *Rev. Mod. Phys.*, Vol. 60, (1988), 3.
42. R. Krause-Rehberg and H.S Leipner, *Positron annihilation in semiconductors-Defects studies*, Springer, Berlin, 1999.
43. A. Vehanen, K. Saarinen, P. Hautojärvi, and H. Huomo, *Phys. Rev. B*35, (1987), 4606.
44. C. Corbel, P. Hautojärvi, J. Märkin, A. Vehanen, D. Mathiot, *J. Phys. Cond. Mat* 1 (1989), 6315.
45. D.T. Britton, P. Willutzki, W. Triftshäuser, E. Hammerl, W. Hansch, I. Eisele, *Appl. Phys.* A58 (1994), 389.
46. S. Eichler, C. Hubner, R. Krause Rehberg, *Appl. Surf. Sci.* 116 (1987), 155.
47. W. Brandt, R. Paulin, *Phys. Rev. B*5 (1972), 2430
48. P. Coleman, *Positron beams and their applications*, World Scientific, Singapore 1999.
49. L Henry, *Structure atomique et activité électrique des défauts natifs et induits par irradiation dans le carbure de silicium 6H-SiC déterminées par annihilation des positrons*, thesis.
50. D.T. Britton, M. Härting, M.B.R. Teemane, S. Mills, F.M. Nortier, and T.N. Van der Walt, *Appl. Surf. Sci.* 116, (1997), 58.
51. D.T. Britton, W. Triftshäuser, W. Bauer-Kugelmann, and D. Knoesen, *Nucl. Inst. Meth.* B164,1010 (2001).

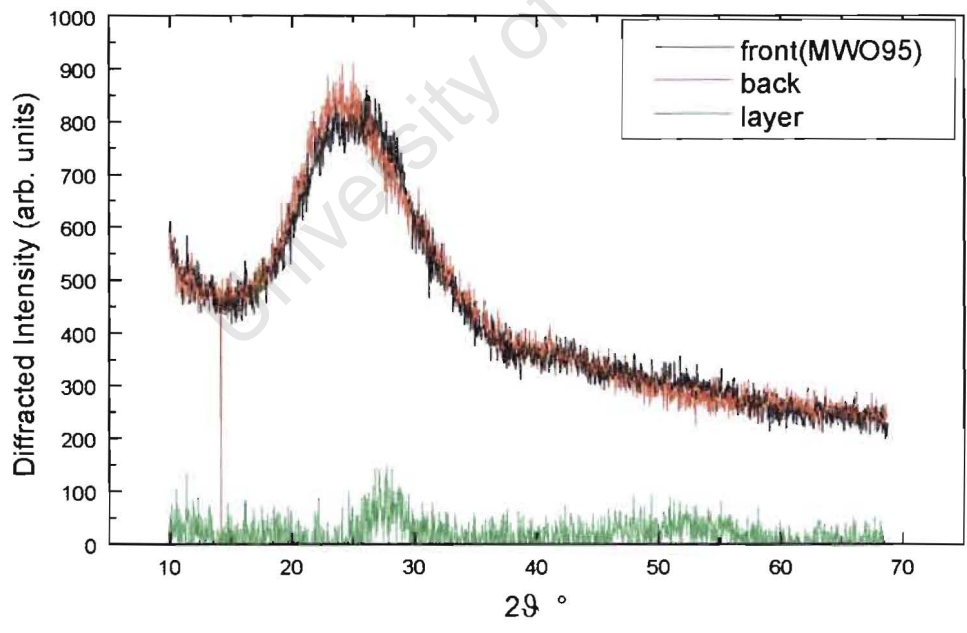
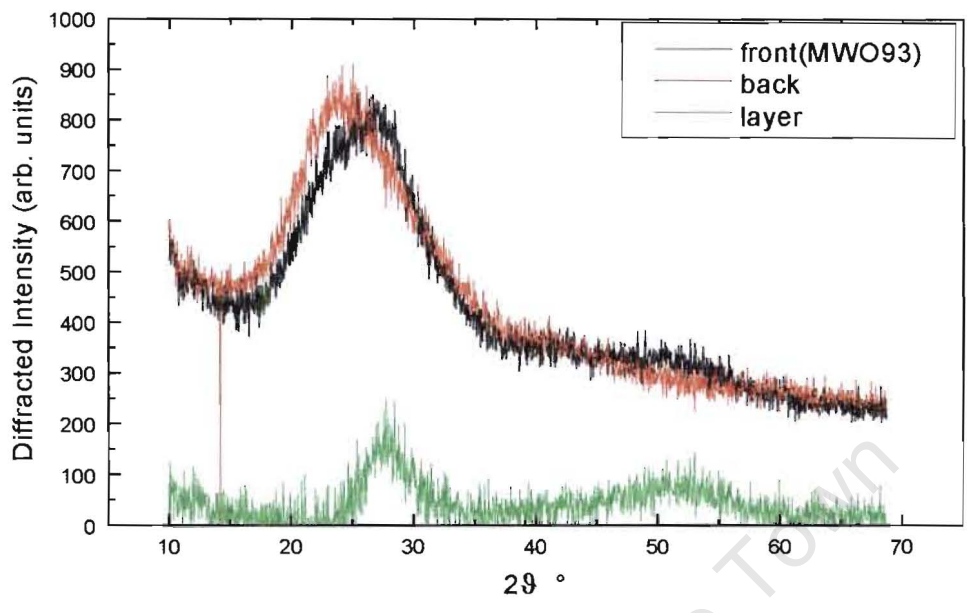
52. A.H. Mahan, J. Yang, S. Guha, D.L. Williamson, Phys. Rev. B61,(2000), 1677.
53. A.H. Mahan, D.L. Williamson, and T.E. Furtak, MRS Symposium proceedings 467(1997), 657.
54. M. Härting, D.T. Britton, E. Minani, A. Hempel, M. Hempel, T.P. Ntsoane, and D. Knoesen., J. Non-Cryst. Solids, 103 (2002), 299.

University of Cape Town

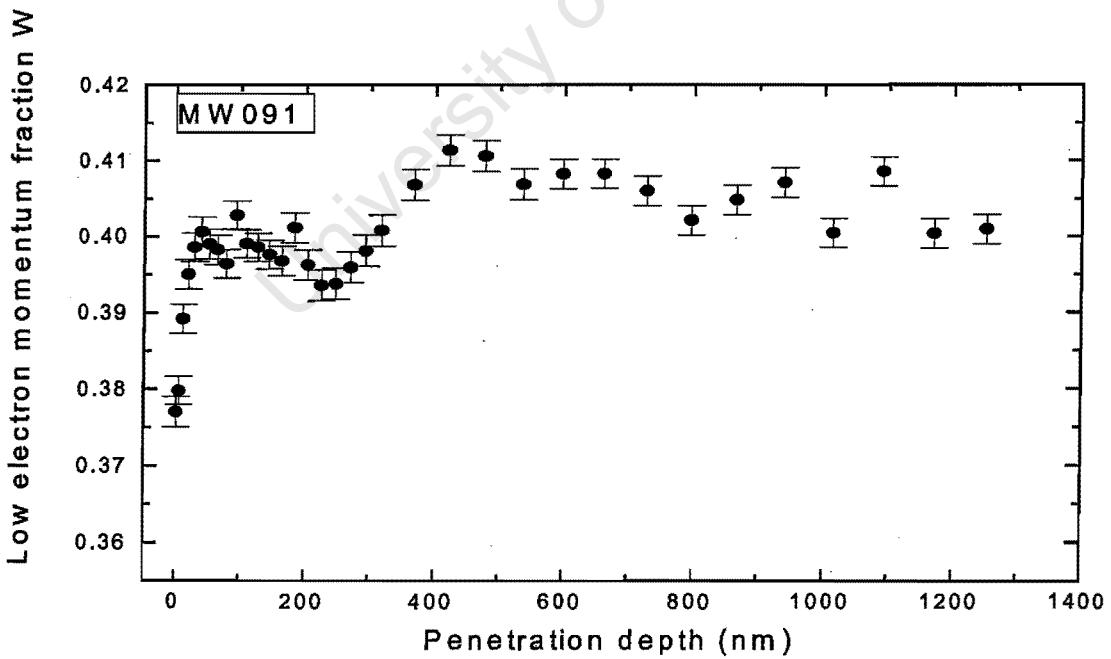
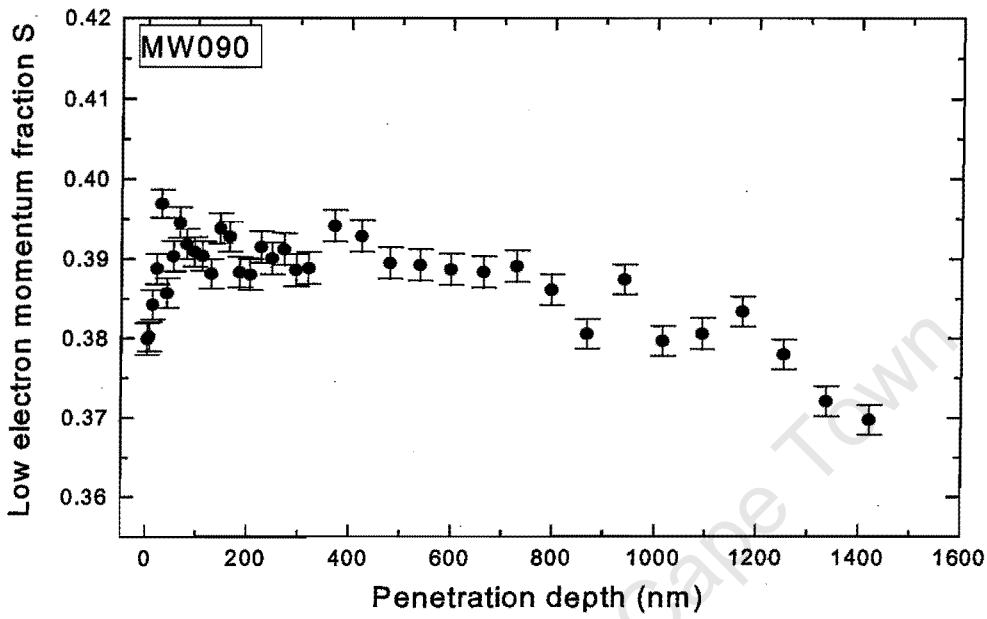
# APPENDIX

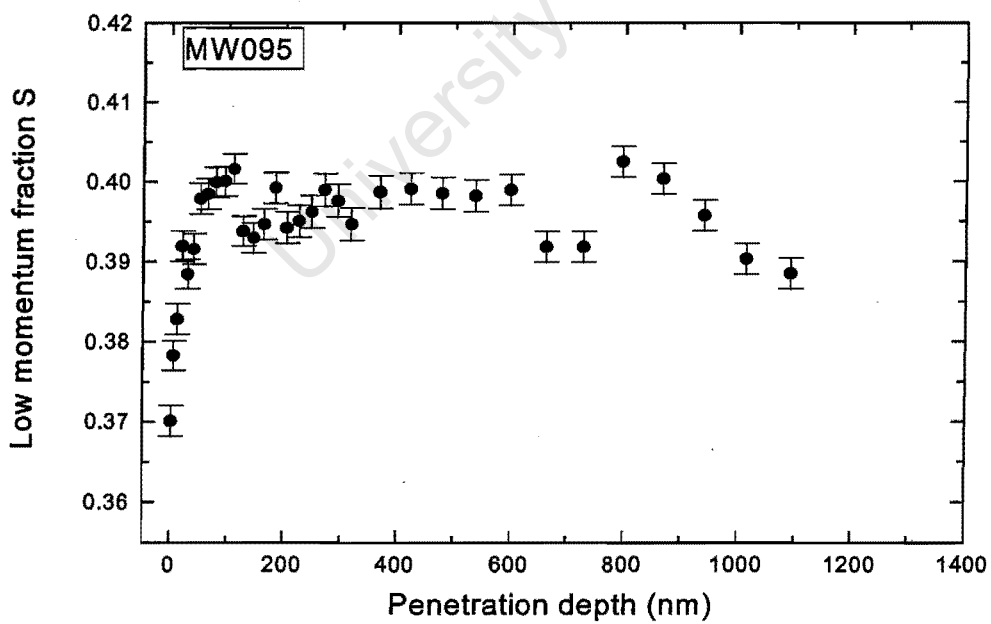
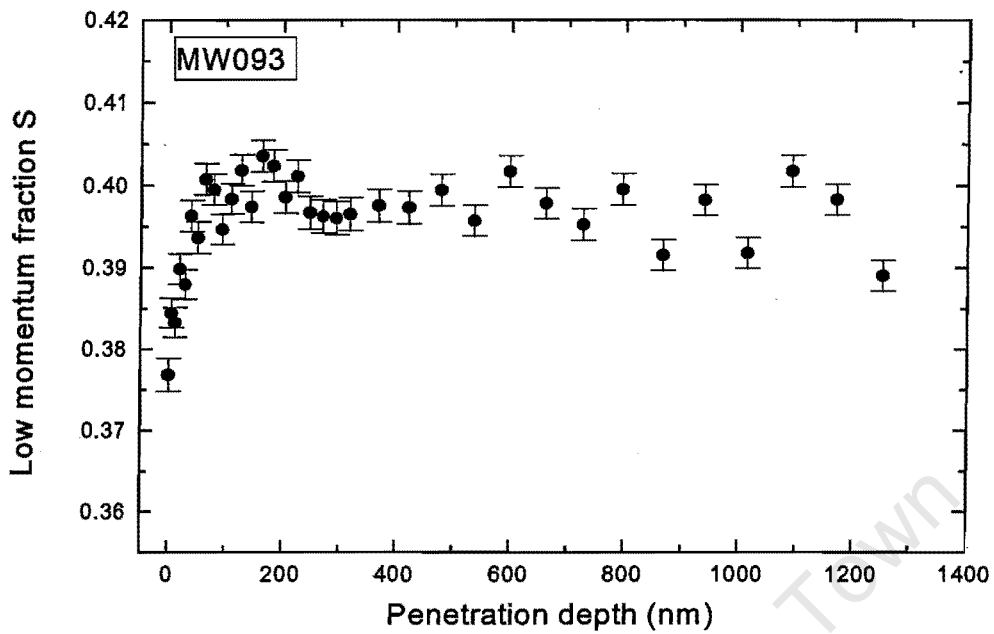
## A.X-RAY DIFFRACTION PATTERNS FOR THE SAMPLES ANALYSED



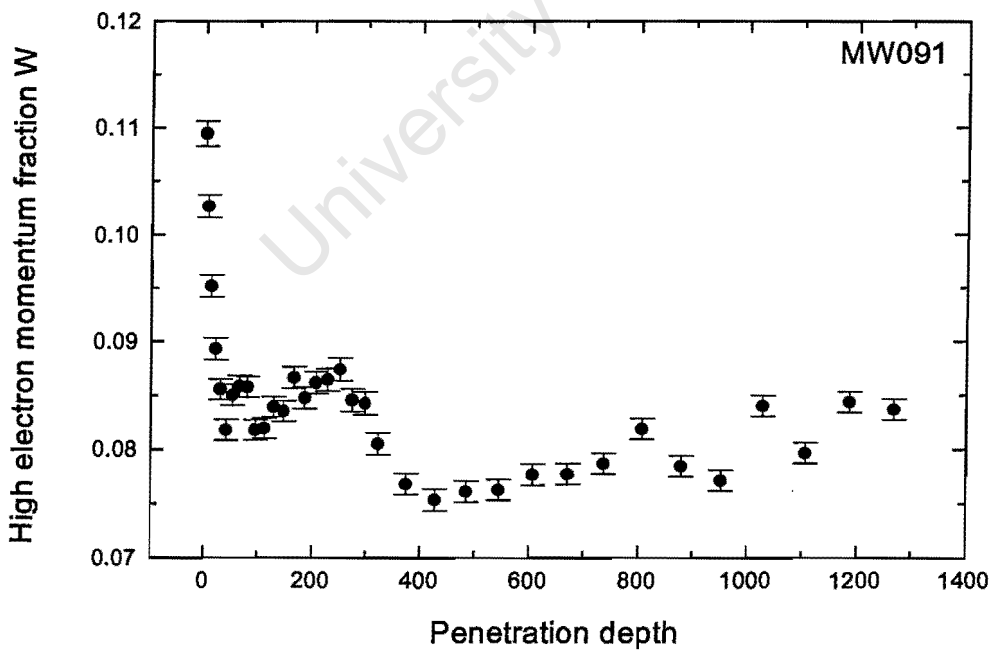
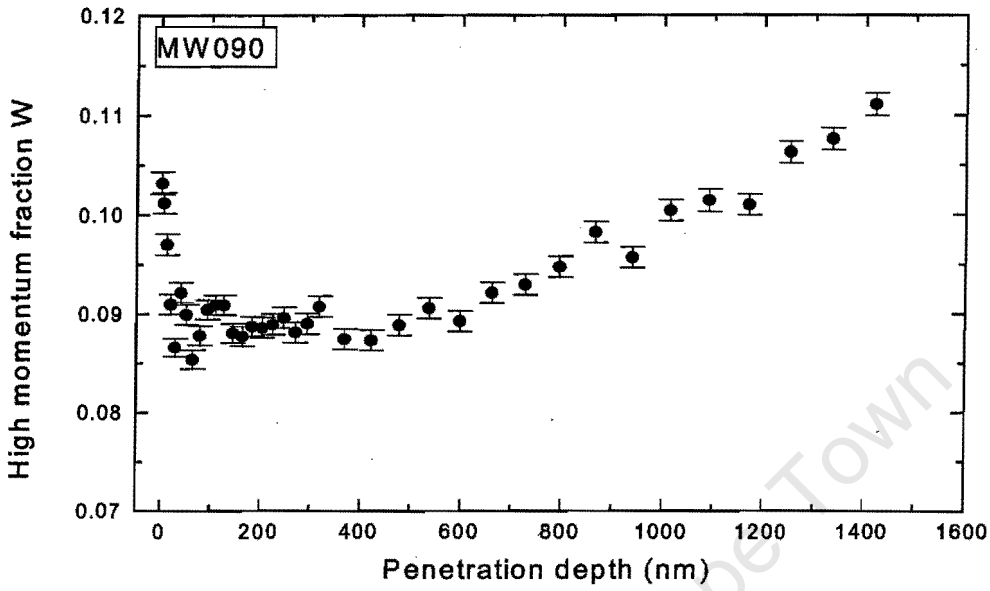


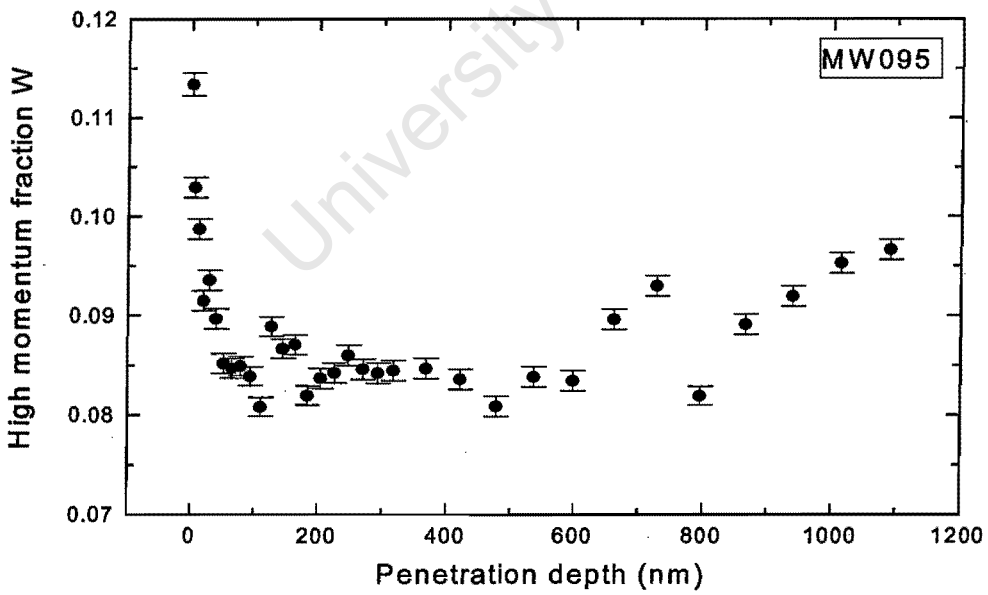
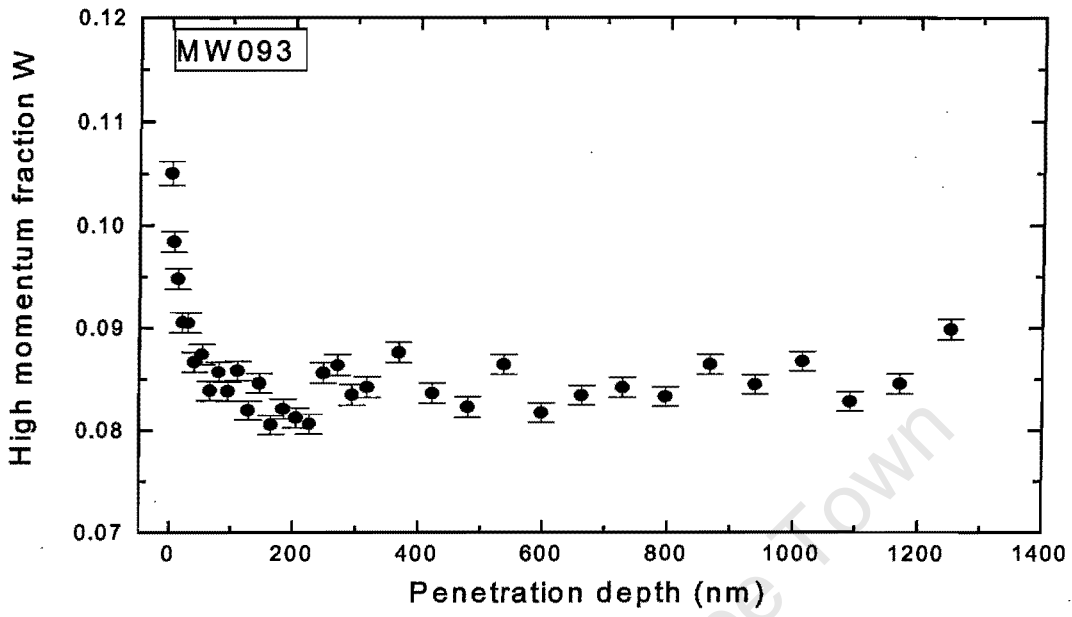
**B. THE LOW MOMENTUM FRACTIONS  $S$  AS FUNCTION OF THE PENETRATION DEPTH FOR ALL SAMPLES USED IN THIS STUDY**





### C. THE HIGH MOMENTUM FRACTION $W$ AS A FUNCTION OF THE PENETRATION DEPTH FOR ALL SAMPLES





**D.THE DIAGRAM OF S VS W FOR ALL THE SAMPLES.**

